machines

MDPI

Article

Dynamic Modeling and Performance Analysis of a Novel Dual-Platform Biped Robot Based on a 4-UPU Parallel Mechanism

Zhaofeng Shi [1], Shengtao Song [1,2,*], Ruiqin Li [1], Fengping Ning [1], Lei Zhang [1] and Lianzheng Deng [1]

[1] School of Mechanical Engineering, North University of China, Taiyuan 030051, China; s202402042@st.nuc.edu.cn (Z.S.)
[2] College of Aeronautics and Astronautics, Taiyuan University of Technology, Taiyuan 030024, China
* Correspondence: nucsst@139.com

Abstract

Biped robots based on parallel mechanisms hold great potential for applications in complex terrains. Based on a 4-UPU parallel mechanism, this paper proposes a novel biped robot that achieves alternating bipedal locomotion and turning with only six actuators by employing fixed/moving platform switching and following an "upper platform + lower foot" continuous gait strategy. Using the influence coefficient method, the first order and second order kinematic influence coefficient matrices of the biped robot were derived. Based on the principle of virtual work, a dynamic model of the robot was formulated, and its validity was verified through numerical simulations. The dynamic performance of the robot was further evaluated using the Dynamic Manipulability Ellipsoid (DME) index, while its stability during step-climbing and turning was analyzed using the Zero-Moment Point (ZMP) method. The results demonstrate that the dual-platform biped robot features a rational structure and exhibits robust stability during step-climbing and turning.

Keywords: biped robot; 4-UPU parallel mechanism; dynamics; dynamic manipulability ellipsoid; stability

check for updates

Academic Editor: Raffaele Di Gregorio

Received: 28 October 2025
Revised: 21 November 2025
Accepted: 25 November 2025
Published: 26 November 2025

Citation: Shi, Z.; Song, S.; Li, R.; Ning, F.; Zhang, L.; Deng, L. Dynamic Modeling and Performance Analysis of a Novel Dual-Platform Biped Robot Based on a 4-UPU Parallel Mechanism. *Machines* **2025**, *13*, 1094. https://doi.org/10.3390/machines13121094

Copyright: © 2025 by the authors. Licensee MDPI, Basel, Switzerland. This article is an open access article distributed under the terms and conditions of the Creative Commons Attribution (CC BY) license (https://creativecommons.org/licenses/by/4.0/).

1. Introduction

Mobile robotics is an interdisciplinary technology that integrates mechanism science, modern control theory, computer science, and artificial intelligence [1]. With the rapid advancement of this technology, mobile robots have played a pivotal role in diverse scenarios such as military reconnaissance, post-disaster rescue, geological exploration, environmental monitoring, and planetary exploration [2–6], enabling them to substitute for humans in accomplishing tasks under highly demanding, hazardous, or extreme environments [7,8].

Among various types of mobile robots, biped robots are of particular interest because they have advantages such as fewer actuated joints, lower energy consumption, stronger environmental adaptability [9,10], larger ranges of motion, and greater locomotion flexibility [11,12]. However, they also face significant challenges, such as insufficient structural stability, weaker dynamic balance, higher inertia, and relatively low load-to-weight ratios [13,14].

The leg mechanism, as one of the core mechanical structures of biped robots, directly determines the robot's motion performance [15,16]. At present, most biped robots employ identical structures for both legs, typically constructed from two identical linkage or serial mechanisms, while some adopt parallel mechanisms to improve load-bearing

capacity [17,18]. Sugahara et al. [19] developed a WL-16RIV robot employing two Stewart mechanisms as the core leg structures, which is capable of stable walking on complex terrains. Wang et al. [20] proposed a parallel-legged biped robot based on a five-link double-crank mechanism, capable of multiple motion modes such as walking, turning, and jumping. Tazaki [21] introduced a biped robot with a 6-RSS parallel mechanism, whose link arrangement is similar to that of a 6-SPS double-triangle mechanism, thereby enlarging the rotation range and improving operational performance while maintaining high position-tracking accuracy under high-frequency motions. Gim et al. [22] designed a hybrid legged biped robot with six degrees of freedom (DOF), which offers a large workspace and high mobility but a relatively weak load-bearing capacity. Xia et al. [23] developed a humanoid-leg biped robot based on a generalized parallel mechanism, featuring low inertia, multiple DOF, and high stiffness. Zhang et al. [13] proposed a four-DOF biped robot with low inertia, a high load-to-weight ratio, and impact resistance, capable of agile operations in confined spaces. Overall, although these robots can achieve complex motions such as walking and step climbing in different environments, they generally rely on dual parallel mechanisms, leading to drawbacks including excessive numbers of mechanisms and actuators and relatively monotonous walking patterns. Here, "R", "P", and "S" denote the revolute joint, prismatic joint, and spherical joint, respectively.

On the other hand, multi-platform mobile robots [24], through distributed load-bearing structures designs, exhibit high stiffness, structural stability, and strong load-carrying capacity. Ren et al. [25] proposed a triple-platform biped robot based on a 6-UPS parallel mechanism, which demonstrated excellent structural stability and dynamic balance capability. Li et al. [26], using an R+2-UPU/2-RPR hybrid mechanism, developed a dual-platform hexapod climbing robot named "XuanGui", primarily designed to replace porters in mountain scenic areas for transporting heavy loads. This robot exhibits strong terrain adaptability and exceptional load-carrying capacity. Nevertheless, while such designs significantly enhance the load-carrying capacity and stability of legged robots, they inevitably restrict motion flexibility to some extent. In summary, the advantages and limitations of current biped robots are highly pronounced, as outlined in Table 1.

Table 1. Characteristics of current biped robots.

Biped Robot	DOF	Number of Actuators	Leg Mechanism Type	Gait Characteristics
WL-16RIV robot	6	12	Dual-parallel mechanism	By using a continuous "foot–platform–foot" gait pattern, the robot achieves a wide range of application scenarios.
MPLBR robot	3	6	Dual-parallel mechanism	By using a continuous "foot–platform–foot" gait pattern, the robot can also perform various maneuvers such as jumping.
Biped robot based on 6-RSS parallel mechanism	6	12	Dual-parallel mechanism	By using a continuous "foot–platform–foot" gait pattern, the robot achieves high position-tracking accuracy.
Biped robot with hybrid leg mechanism	6	12	Dual-parallel mechanism	By using a continuous "foot–platform–foot" gait pattern, the robot achieves a large workspace.
Humanoid-leg biped robot based on generalized parallel mechanism	6	12	Dual-parallel mechanism	By using a continuous "foot–platform–foot" gait pattern, the robot exhibits low motion inertia.
Four-DOF biped robot	4	8	Dual-parallel mechanism	By using a continuous "foot–platform–foot" gait pattern, the robot is suitable for maneuvering in confined spaces.
Triple-platform biped robot	6	12	Dual-parallel mechanism	By using a continuous "upper platform + lower foot" gait pattern, but the involvement of two moving platforms makes the walking process somewhat more complex.
Dual-platform biped robot (proposed)	4	6	Single-parallel mechanism	By continuously switching between a moving and fixed platform, the robot achieves a continuous "upper platform + lower foot" gait pattern for locomotion.

Given that current biped robot configurations tend to be structurally fixed, require many mechanisms and actuated joints, and exhibit relatively constrained walking modes, it is of practical significance to develop a novel biped robot that integrates the advantages of multi-platform architectures with those of conventional biped structures. The main

contribution of this paper is the proposal of a dual-platform biped robot and conducting a theoretical analysis, which lays the foundation for subsequent control system design and prototype development. By continuously switching between the moving platform and fixed platform within a single parallel mechanism, the dual-platform biped robot achieves a continuous "upper + lower" alternating gait with relatively few actuated joints. This design effectively reduces structural complexity and enables locomotion over challenging terrains such as pits, crevices, steps, and bends in hazardous underground spaces, supporting tasks like inspection and manipulation.

The remainder of this paper is organized as follows: In Section 2, the structural design and gait pattern of the dual-platform biped robot are introduced, and the velocity and acceleration mapping between the moving components and the actuated joints are established using the influence coefficient method. In Section 3, the force distribution of the mechanical components is analyzed and based on the velocities and accelerations of all moving links, the robot's dynamic model is formulated using the principle of virtual work, followed by numerical simulations to validate its accuracy. In Section 4, relying on the validated dynamic model, the dynamic manipulability ellipsoid is employed to evaluate the isotropy of the robot's acceleration capability. In Section 5, to further evaluate the dynamic stability of the biped robot, simulations of its step-climbing and turning process are conducted, and the robot's dynamic stability during these motion processes is analyzed based on the Zero Moment Point theory. Conclusions are drawn in Section 6.

2. Kinematic Analysis

2.1. Mechanism Overview

The overall structure of the dual-platform biped robot is illustrated in Figure 1. Platform I is connected to Foot I through UPU branch chains III and IV and to Foot II through P branch chain I, while Platform II is connected to Foot I through P branch chain II and to Foot II through UPU branch chains I and II. Unlike conventional biped robots that employ two independent and identical parallel legs, the dual-platform biped robot incorporates Platform II as a connecting component between the two legs, thereby forming a structurally asymmetric dual-platform biped configuration. This design not only conforms to the characteristics of multi-platform structures but also provides a reliable structural foundation for realizing the robot's unique locomotion mode. Here, "U" denotes the universal joint.

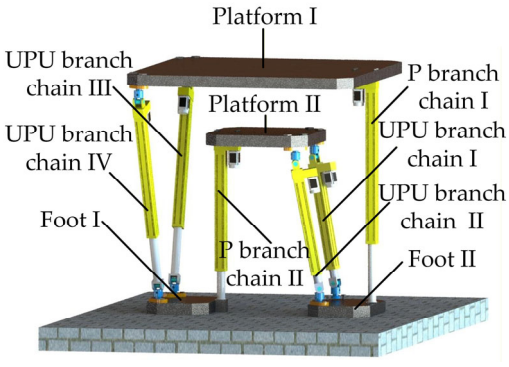


Figure 1. Structural design of dual-platform biped robot.

Based on this structural configuration, when the robot performs a leg-lifting motion, the P branch chains I and II are actuated simultaneously to realize the vertical movement of the "upper platform + lower foot", as shown in Figure 2a. During the double-support phase, the P branch chains I and II can each be combined with the four UPU branch chains to form two 2-UPU/P parallel mechanisms, which are employed to fine-tune the distance between Platform I and Platform II, as illustrated in Figure 2b. Moreover, at all other moments of

the robot's motion, the P branch chains of the dual-platform biped robot remain locked. Consequently, during locomotion, Platform I, P branch chain I, and Foot II can be regarded as one rigid unit, while Platform II, P branch chain II, and Foot I constitute another rigid unit. These two rigid units correspond to the fixed and moving platform of the 4-UPU parallel mechanism, as shown in Figure 2c. In the figure, the red and blue rectangles, respectively, represent the fixed platform and the moving platform.

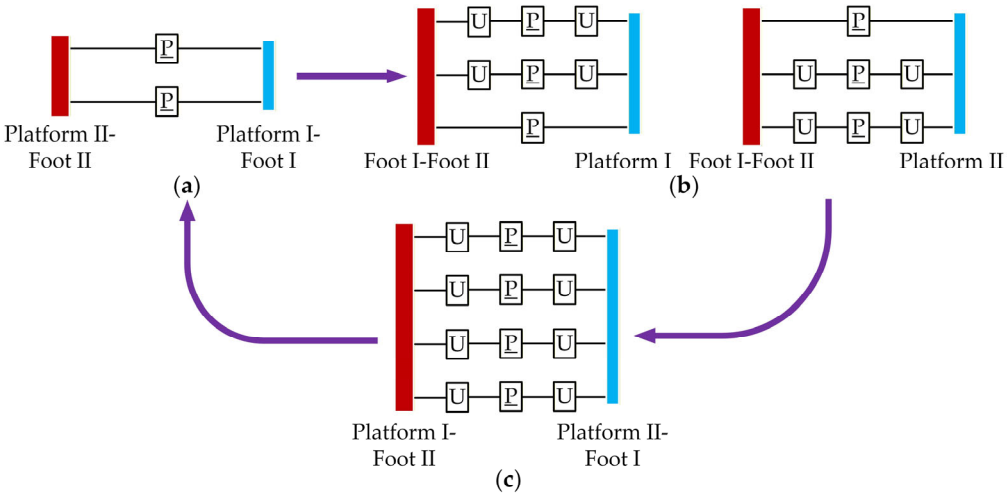


Figure 2. Transformation process of the topology diagram of the dual-platform biped robot: (**a**) 2-P parallel mechanism; (**b**) 2-UPU/P parallel mechanism; and (**c**) 4-UPU parallel mechanism. (P represents driven joints).

Building upon the above actuation and locking switching mechanism of the P branch chains, the gait characteristics of the dual-platform biped robot can be described as follows. Unlike the continuous gait of conventional biped robots, which follows a "foot–platform–foot" sequential walking pattern, the dual-platform biped robot achieves a coordinated "upper + lower" continuous gait through this mechanism. This gait is specifically characterized by the fact that, when the robot performs foot-end motions such as lifting, advancing, sidestepping, turning, and descending, one set of "upper platform + lower foot" always moves in coordination. Such a "platform–foot" coordinated structural mode simplifies the walking process and improves locomotion efficiency.

2.2. Position Analysis

Before analyzing the velocity and acceleration of the dual-platform biped robot, local coordinate systems are established for both platforms and feet, so that the spatial coordinates of each joint can be determined. In the initial pose, the geometric central axes of Platform I and Platform II coincide. The coordinate system $\{O_1\}$ is defined at the geometric center of Platform I, where the Z_1 axis points upward, perpendicular to Platform I, the X_1 axis is parallel to the line A_3A_4, and the Y_1 axis is determined by the right-hand rule. Similarly, coordinate systems $\{O_2\}$, $\{O_3\}$, and $\{O_4\}$ are established at the geometric centers of Platform II, Foot I, and Foot II, respectively, with their axes kept parallel to those of $\{O_1\}$. The coordinate distributions are illustrated in Figure 3. Platform I and Platform II are square structures with side lengths of 2a and 2b, respectively, while Foot I and Foot II are identical rectangles of size 2c × 2d. Here, the lengths of UPU branch chains I and II are 135–215 mm, UPU branch chains III and IV are 170–275 mm, P branch chain I is 155–260 mm, and P branch chain II is 130–210 mm. In the figure, S_{ij} denotes the motion direction of the j-th kinematic pair of the UPU branch chain i.

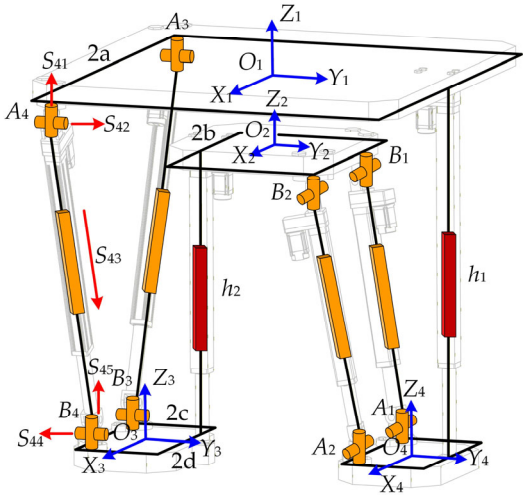


Figure 3. Schematic diagram of the mechanism.

When the two P branch chains are in a locked state, the robot is essentially equivalent to a 4-UPU parallel mechanism. In this case, the alternating motion of the biped corresponds to the continuous switch between the moving and fixed platforms of the 4-UPU parallel mechanism. Since the theory's framework and analytical method are identical regardless of which component is chosen as the moving platform, this paper takes Foot I as the moving platform and Foot II as the fixed platform for analysis.

In the fixed coordinate system $\{O_4\}$, the coordinates of the joints A_i (i = 1, 2, 3, 4) are given by

$$\begin{cases} \boldsymbol{A}_1 = (-\mathrm{d}, -\mathrm{c}, 0)^{\mathrm{T}} \\ \boldsymbol{A}_2 = (\mathrm{d}, -\mathrm{c}, 0)^{\mathrm{T}} \\ \boldsymbol{A}_3 = (-\mathrm{a}, \mathrm{c}-2\mathrm{a}, \mathrm{Z}+h_1)^{\mathrm{T}} \\ \boldsymbol{A}_4 = (\mathrm{a}, \mathrm{c}-2\mathrm{a}, \mathrm{Z}+h_1)^{\mathrm{T}} \end{cases} \tag{1}$$

where h_1 denotes the length of P branch chain I under different initial poses.

In the moving coordinate system $\{O_3\}$, the coordinates of the joints B_i (i = 1, 2, 3, 4) are given by

$$\begin{cases} \boldsymbol{b}_1 = (-\mathrm{b}, 2\mathrm{b}+\mathrm{c}, h_2 - Z)^{\mathrm{T}} \\ \boldsymbol{b}_2 = (\mathrm{b}, 2\mathrm{b}+\mathrm{c}, h_2 - Z)^{\mathrm{T}} \\ \boldsymbol{b}_3 = (-\mathrm{d}, -\mathrm{c}, 0)^{\mathrm{T}} \\ \boldsymbol{b}_4 = (\mathrm{d}, -\mathrm{c}, 0)^{\mathrm{T}} \end{cases} \tag{2}$$

where h_2 denotes the length of P branch chain II under different initial poses.

In this paper, the Z–Y–X Euler angle convention is adopted to describe the orientation of the coordinate system $\{O_3\}$ with respect to the coordinate system $\{O_4\}$. Since the 4-UPU parallel mechanism is a four-DOF mechanism, which enables translational motion in three-dimensional space together with rotation about the Z-axis [27]. As a result, the mechanism does not encounter the kinematic singularities that may arise when Z–Y–X Euler angles are used. Let α denote the rotation angle of Foot I about the Z_3 axis. The corresponding rotation matrix $\boldsymbol{R}$ can be expressed as

$$\boldsymbol{R} = \begin{bmatrix} \mathrm{c}\alpha & -\mathrm{s}\alpha & 0 \\ \mathrm{s}\alpha & \mathrm{c}\alpha & 0 \\ 0 & 0 & 1 \end{bmatrix} \tag{3}$$

where $\mathrm{s}\alpha = \sin\alpha$ and $\mathrm{c}\alpha = \cos\alpha$, and similarly hereinafter.

Let the position vector between the moving coordinate system $\{O_3\}$ and the fixed coordinate system $\{O_4\}$ be denoted as $\boldsymbol{P} = (X, Y, Z)^{\mathrm{T}}$. Based on Equation (4), the coordinate transformation is established to map the coordinates of any point in $\{O_3\}$ to $\{O_4\}$.

$$\boldsymbol{B}_i = \boldsymbol{R}\boldsymbol{b}_i + \boldsymbol{P} \tag{4}$$

From Equation (4), the coordinates of all joints in the fixed coordinate system $\{O_4\}$ are obtained, providing the basis for the subsequent analysis of velocity and acceleration.

2.3. Velocity Analysis

There are many methods available for analyzing the velocity and acceleration of parallel mechanisms, among which the most widely adopted include the differentiation method, vector method, screw theory, and influence coefficient method. Thomas and Tesar [28] proposed the use of the influence coefficient method to solve for velocity and acceleration of mechanisms, which intuitively reveals the essence of mechanism kinematics. In addition, the first-order and second-order kinematic influence coefficient matrices established based on the influence coefficient method have simple and clear expressions, are easy to understand, and can be applied to the performance analysis of parallel mechanisms such as singularity, flexibility, load capacity [29], isotropy, and dynamic manipulability [30]. Therefore, this paper employs the influence coefficient method to analyze the velocity and acceleration of the dual-platform biped robot.

When applying the influence coefficient method to solve the velocity mapping relationship between the moving platform and the actuators, it is necessary to establish the velocity relationships between all kinematic pairs on the UPU branch chain i and moving platform. Since the dual-platform biped robot is a lower-DOF mechanism and the number of DOF of the moving platform is not equal to the number of kinematic pairs in UPU branch chain i, it is difficult to directly construct the corresponding influence coefficient matrix. To address this issue, the fictitious mechanism approach is employed, whereby the number of fundamental kinematic pairs in the UPU branch chain i is supplemented to six, and the multi-DOF kinematic pairs in the chain are replaced by single-DOF kinematic pairs. A schematic diagram of the equivalent kinematic pairs of the UPU branch chain i is shown in Figure 3. The motion directions of the kinematic pairs in the UPU branch chain i are therefore given by

$$\boldsymbol{S}_{i1} = \begin{bmatrix} 0 & 0 & 1 \end{bmatrix}^{\mathrm{T}}, \boldsymbol{S}_{i2} = \boldsymbol{S}_{i1} \times \boldsymbol{S}_{i3}, \boldsymbol{S}_{i3} = (\boldsymbol{B}_i - \boldsymbol{A}_i)/|\boldsymbol{B}_i - \boldsymbol{A}_i|, \boldsymbol{S}_{i4} = \boldsymbol{S}_{i2}, \boldsymbol{S}_{i5} = \begin{bmatrix} 0 & 0 & 1 \end{bmatrix}^{\mathrm{T}} \tag{5}$$

Since the fictitious kinematic pairs must combine with the original kinematic pairs in the chain to form six fundamental kinematic pairs, the directions of the fictitious kinematic pairs in the UPU branch chain i are therefore given by

$$\boldsymbol{S}_{i6} = \boldsymbol{S}_{i4} \times \boldsymbol{S}_{i5} \tag{6}$$

Then, the first-order influence coefficient matrix corresponding to each kinematic pair in UPU branch chain i can be expressed as

$$\left[\boldsymbol{G}_{\theta}^{H}\right]^{(i)} = \begin{bmatrix} \boldsymbol{S}_{i1} & \boldsymbol{S}_{i2} & 0 & \boldsymbol{S}_{i4} & \boldsymbol{S}_{i5} & \boldsymbol{S}_{i6} \\ \boldsymbol{S}_{i1} \times (\boldsymbol{P} - \boldsymbol{A}_i) & \boldsymbol{S}_{i2} \times (\boldsymbol{P} - \boldsymbol{A}_i) & \boldsymbol{S}_{i3} & \boldsymbol{S}_{i4} \times (\boldsymbol{P} - \boldsymbol{B}_i) & \boldsymbol{S}_{i5} \times (\boldsymbol{P} - \boldsymbol{B}_i) & \boldsymbol{S}_{i6} \times (\boldsymbol{P} - \boldsymbol{B}_i) \end{bmatrix} \tag{7}$$

The instantaneous velocity of Foot I is represented by a six-dimensional column vector as

$$\boldsymbol{V}_H = \begin{bmatrix} \omega_x & \omega_y & \omega_z & v_x & v_y & v_z \end{bmatrix}^{\mathrm{T}} \tag{8}$$

By combining Equations (7) and (8), the velocity mapping between each kinematic pair of UPU branch chain i and Foot I can be obtained as

$$\boldsymbol{V}_H = \left[\boldsymbol{G}_\theta^H\right]^{(i)} \dot{\boldsymbol{\theta}}^{(i)} \tag{9}$$

where $\dot{\boldsymbol{\theta}}^{(i)}$ represents the velocity of each kinematic pair in UPU branch chain i.

When the matrix $\left[\boldsymbol{G}_\theta^H\right]^{(i)}$ is non-singular (i.e., invertible), the following relation holds:

$$\dot{\boldsymbol{\theta}}^{(i)} = \left[\boldsymbol{G}_H^\theta\right]^{(i)} \boldsymbol{V}_H \tag{10}$$

where $\boldsymbol{G}_H^\theta = \left[\boldsymbol{G}_\theta^H\right]^{-1}$, and similarly hereinafter.

By selecting the prismatic joint in UPU branch chain i as the actuated joint, the velocity mapping relationship between the actuated joints of all UPU branch chains and the moving platform is obtained from Equation (10) as

$$\dot{\boldsymbol{\theta}}_3^{(i)} = \left[\boldsymbol{G}_H^\theta\right]_{3:}^{(i)} \boldsymbol{V}_H \tag{11}$$

where $\dot{\boldsymbol{\theta}}_3^{(i)}$ denotes the velocity of the prismatic joint in the UPU branch chain i, $\left[\boldsymbol{G}_H^\theta\right]_{3:}^{(i)}$. This represents the third row of its corresponding matrix $\left[\boldsymbol{G}_H^\theta\right]^{(i)}$, and similarly hereinafter.

By further rearranging Equation (11) into a matrix form, the overall velocity mapping expression of the biped robot can be obtained as

$$\dot{\boldsymbol{q}} = \boldsymbol{G}_H^q \boldsymbol{V}_H \tag{12}$$

where

$$\dot{\boldsymbol{q}} = \begin{bmatrix} \dot{\theta}_3^{(1)} & \dot{\theta}_3^{(2)} & \dot{\theta}_3^{(3)} & \dot{\theta}_3^{(4)} & 0 & 0 \end{bmatrix}^{\mathrm{T}},\ \boldsymbol{G}_H^q = \begin{bmatrix} \left[\boldsymbol{G}_H^\theta\right]_{3:}^{(1)} & \left[\boldsymbol{G}_H^\theta\right]_{3:}^{(2)} & \left[\boldsymbol{G}_H^\theta\right]_{3:}^{(3)} & \left[\boldsymbol{G}_H^\theta\right]_{3:}^{(4)} & \left[\boldsymbol{G}_H^\theta\right]_{6:}^{(3)} & \left[\boldsymbol{G}_H^\theta\right]_{6:}^{(4)} \end{bmatrix}^{\mathrm{T}}.$$

When matrix $\boldsymbol{G}_H^q$ is invertible, Equation (12) can be further rewritten as

$$\boldsymbol{V}_H = \boldsymbol{G}_q^H \dot{\boldsymbol{q}} \tag{13}$$

where $\boldsymbol{G}_q^H$ denotes the first-order kinematic influence coefficient matrix of the dual-platform biped robot, i.e., the velocity Jacobian matrix.

By substituting Equation (13) into Equation (9), the velocity mapping between the kinematic pairs of UPU branch chain i and the generalized actuators can be obtained as

$$\dot{\boldsymbol{\theta}}^{(i)} = \left[\boldsymbol{G}_q^\theta\right]^{(i)} \dot{\boldsymbol{q}} \tag{14}$$

where $\left[\boldsymbol{G}_q^\theta\right]^{(i)} = \left[\boldsymbol{G}_H^\theta\right]^{(i)} \boldsymbol{G}_q^H$.

To facilitate the establishment of the kinematic model of each link in the dual-platform biped robot, assume that the swing link k_1 and the telescopic link k_2 in UPU branch chain i are both axisymmetric rigid bodies. Since the swing link k_1 rotates about the universal joint A_i, its center-of-mass (CoM) velocity $\boldsymbol{V}_{k1}^{(i)}$ can be derived from Equation (9) as

$$\boldsymbol{V}_{k1}^{(i)} = \left[\boldsymbol{G}_\theta^{k1}\right]^{(i)} \dot{\boldsymbol{\theta}}_{k1}^{(i)} \tag{15}$$

where $V_{k1}^{(i)} = \begin{bmatrix} \omega_{k1x} & \omega_{k1y} & \omega_{k1z} & v_{k1x} & v_{k1y} & v_{k1z} \end{bmatrix}^{\mathrm{T}}$, $\left[G_{\theta}^{k1}\right]^{(i)} = \begin{bmatrix} S_{i1} & S_{i2} \\ S_{i1} \times (P_{k1}^{(i)} - A_i) & S_{i2} \times (P_{k1}^{(i)} - A_i) \end{bmatrix}$, $P_{k1}^{(i)}$ denotes the position of the CoM of the swinging link k_1 of the UPU branch chain i, similarly hereinafter.

By substituting Equation (14) into Equation (15), the velocity mapping between the swing link k_1 and the generalized actuators can be further obtained as

$$V_{k1}^{(i)} = \left[G_{\theta}^{k1}\right]^{(i)} \left[G_{q}^{\theta}\right]_{1:,2:}^{(i)} \dot{q} = \left[G_{q}^{k1}\right]^{(i)} \dot{q} \tag{16}$$

Here, $\left[G_{q}^{\theta}\right]_{1:,\,2:}^{(i)}$ represents the first and second row of its corresponding matrix $\left[G_{q}^{\theta}\right]^{(i)}$, and similarly hereinafter.

Compared with the swing link k_1, the telescopic link k_2 not only rotates about the universal joint A_i but also translates along the direction of B_iA_i. Accordingly, its CoM velocity $V_{k2}^{(i)}$ can be expressed as

$$V_{k2}^{(i)} = \left[G_{\theta}^{k2}\right]^{(i)} \dot{\theta}_{k2}^{(i)} \tag{17}$$

where $V_{k2}^{(i)} = \begin{bmatrix} \omega_{k2x} & \omega_{k2y} & \omega_{k2z} & v_{k2x} & v_{k2y} & v_{k2z} \end{bmatrix}^{\mathrm{T}}$, $\left[G_{\theta}^{k2}\right]^{(i)} = \begin{bmatrix} S_{i1} & S_{i2} & 0 \\ S_{i1} \times (P_{k2}^{(i)} - A_i) & S_2 \times (P_{k2}^{(i)} - A_i) & S_{i3} \end{bmatrix}$.

By analogy, substituting Equation (14) into Equation (17) yields the velocity mapping between the telescopic link k_2 and the generalized actuations as

$$V_{k2}^{(i)} = \left[G_{\theta}^{k2}\right]^{(i)} \left[G_{q}^{\theta}\right]_{1:,\,2:,\,3:}^{(i)} \dot{q} = \left[G_{q}^{k2}\right]^{(i)} \dot{q} \tag{18}$$

2.4. Acceleration Analysis

Determining the acceleration of all moving components is fundamental to constructing the dynamic model of the dual-platform biped robot. Building upon the velocity analysis in Section 2.3, a second time differentiation of the velocity expressions directly yields the accelerations of both the actuators and linkage members in each branch chain.

By differentiating both sides of Equation (9) with respect to time, the acceleration of Foot I, denoted as A_H, is obtained.

$$A_H = \left[\dot{\theta}^{(i)}\right]^{\mathrm{T}} \left[H_{\theta}^{H}\right]^{(i)} \dot{\theta}^{(i)} + \left[G_{\theta}^{H}\right]^{(i)} \ddot{\theta}^{(i)} \tag{19}$$

where $A_H = \begin{bmatrix} \varepsilon_x & \varepsilon_y & \varepsilon_z & a_x & a_y & a_z \end{bmatrix}^{\mathrm{T}}$, H_{θ}^{H} is a 6×6 vector matrix, i.e., $H_{\theta}^{H} \in R^{6\times6\times6}$, $\ddot{\theta}^{(i)}$ represents the acceleration of each kinematic pair in UPU branch chain i.

Accordingly, the row vectors of the second-order derivative matrix $\left[H_{\theta}^{H}\right]^{(i)}$ of the UPU branch chain i can be expressed as follows:

$$
\begin{aligned}
[\boldsymbol{H}_{\theta}^{H}]_{1::}^{(i)} &= \begin{bmatrix} \mathbf{0} & \boldsymbol{S}_{i1}\times\boldsymbol{S}_{i2} & \mathbf{0} & \boldsymbol{S}_{i1}\times\boldsymbol{S}_{i4} & \boldsymbol{S}_{i1}\times\boldsymbol{S}_{i5} & \boldsymbol{S}_{i1}\times\boldsymbol{S}_{i6} \\ \boldsymbol{S}_{i1}\times[\boldsymbol{S}_{i1}\times(\boldsymbol{P}-\boldsymbol{A}_i)] & \boldsymbol{S}_{i1}\times[\boldsymbol{S}_{i2}\times(\boldsymbol{P}-\boldsymbol{A}_i)] & \boldsymbol{S}_{i1}\times\boldsymbol{S}_{i3} & \boldsymbol{S}_{i1}\times[\boldsymbol{S}_{i4}\times(\boldsymbol{P}-\boldsymbol{B}_i)] & \boldsymbol{S}_{i1}\times[\boldsymbol{S}_{i5}\times(\boldsymbol{P}-\boldsymbol{B}_i)] & \boldsymbol{S}_{i1}\times[\boldsymbol{S}_{i6}\times(\boldsymbol{P}-\boldsymbol{B}_i)] \end{bmatrix} \\
[\boldsymbol{H}_{\theta}^{H}]_{2::}^{(i)} &= \begin{bmatrix} \mathbf{0} & \mathbf{0} & \mathbf{0} & \boldsymbol{S}_{i2}\times\boldsymbol{S}_{i4} & \boldsymbol{S}_{i2}\times\boldsymbol{S}_{i5} & \boldsymbol{S}_{i2}\times\boldsymbol{S}_{i6} \\ \boldsymbol{S}_{i1}\times[\boldsymbol{S}_{i2}\times(\boldsymbol{P}-\boldsymbol{A}_i)] & \boldsymbol{S}_{i2}\times[\boldsymbol{S}_{i2}\times(\boldsymbol{P}-\boldsymbol{A}_i)] & \boldsymbol{S}_{i2}\times\boldsymbol{S}_{i3} & \boldsymbol{S}_{i2}\times[\boldsymbol{S}_{i4}\times(\boldsymbol{P}-\boldsymbol{B}_i)] & \boldsymbol{S}_{i2}\times[\boldsymbol{S}_{i5}\times(\boldsymbol{P}-\boldsymbol{B}_i)] & \boldsymbol{S}_{i2}\times[\boldsymbol{S}_{i6}\times(\boldsymbol{P}-\boldsymbol{B}_i)] \end{bmatrix} \\
[\boldsymbol{H}_{\theta}^{H}]_{3::}^{(i)} &= \begin{bmatrix} \mathbf{0} & \mathbf{0} & \mathbf{0} & \mathbf{0} & \mathbf{0} & \mathbf{0} \\ \boldsymbol{S}_{i1}\times\boldsymbol{S}_{i3} & \boldsymbol{S}_{i2}\times\boldsymbol{S}_{i3} & \mathbf{0} & \mathbf{0} & \mathbf{0} & \mathbf{0} \end{bmatrix} \\
[\boldsymbol{H}_{\theta}^{H}]_{4::}^{(i)} &= \begin{bmatrix} \mathbf{0} & \mathbf{0} & \mathbf{0} & \mathbf{0} & \boldsymbol{S}_{i4}\times\boldsymbol{S}_{i5} & \boldsymbol{S}_{i4}\times\boldsymbol{S}_{i6} \\ \boldsymbol{S}_{i1}\times[\boldsymbol{S}_{i4}\times(\boldsymbol{P}-\boldsymbol{B}_i)] & \boldsymbol{S}_{i2}\times[\boldsymbol{S}_{i4}\times(\boldsymbol{P}-\boldsymbol{B}_i)] & \mathbf{0} & \boldsymbol{S}_{i4}\times[\boldsymbol{S}_{i4}\times(\boldsymbol{P}-\boldsymbol{B}_i)] & \boldsymbol{S}_{i4}\times[\boldsymbol{S}_{i5}\times(\boldsymbol{P}-\boldsymbol{B}_i)] & \boldsymbol{S}_{i4}\times[\boldsymbol{S}_{i6}\times(\boldsymbol{P}-\boldsymbol{B}_i)] \end{bmatrix} \\
[\boldsymbol{H}_{\theta}^{H}]_{5::}^{(i)} &= \begin{bmatrix} \mathbf{0} & \mathbf{0} & \mathbf{0} & \mathbf{0} & \mathbf{0} & \boldsymbol{S}_{i5}\times\boldsymbol{S}_{i6} \\ \boldsymbol{S}_{i1}\times[\boldsymbol{S}_{i5}\times(\boldsymbol{P}-\boldsymbol{B}_i)] & \boldsymbol{S}_{i2}\times[\boldsymbol{S}_{i5}\times(\boldsymbol{P}-\boldsymbol{B}_i)] & \mathbf{0} & \boldsymbol{S}_{i4}\times[\boldsymbol{S}_{i5}\times(\boldsymbol{P}-\boldsymbol{B}_i)] & \boldsymbol{S}_{i5}\times[\boldsymbol{S}_{i5}\times(\boldsymbol{P}-\boldsymbol{B}_i)] & \boldsymbol{S}_{i5}\times[\boldsymbol{S}_{i6}\times(\boldsymbol{P}-\boldsymbol{B}_i)] \end{bmatrix} \\
[\boldsymbol{H}_{\theta}^{H}]_{6::}^{(i)} &= \begin{bmatrix} \mathbf{0} & \mathbf{0} & \mathbf{0} & \mathbf{0} & \mathbf{0} & \mathbf{0} \\ \boldsymbol{S}_{i1}\times[\boldsymbol{S}_{i6}\times(\boldsymbol{P}-\boldsymbol{B}_i)] & \boldsymbol{S}_{i2}\times[\boldsymbol{S}_{i6}\times(\boldsymbol{P}-\boldsymbol{B}_i)] & \mathbf{0} & \boldsymbol{S}_{i4}\times[\boldsymbol{S}_{i6}\times(\boldsymbol{P}-\boldsymbol{B}_i)] & \boldsymbol{S}_{i5}\times[\boldsymbol{S}_{i6}\times(\boldsymbol{P}-\boldsymbol{B}_i)] & \boldsymbol{S}_{i6}\times[\boldsymbol{S}_{i6}\times(\boldsymbol{P}-\boldsymbol{B}_i)] \end{bmatrix}
\end{aligned} \tag{20}
$$

By substituting Equation (14) into Equation (19) and simplifying, the following relation is obtained:

$$\ddot{\boldsymbol{\theta}}^{(i)} = \left[\boldsymbol{G}_H^{\theta}\right]^{(i)}\boldsymbol{A}_H - \dot{\boldsymbol{q}}^{\mathrm{T}}\boldsymbol{L}^{(i)}\dot{\boldsymbol{q}} \tag{21}$$

where $\boldsymbol{L}^{(i)} = \begin{bmatrix} \left[\boldsymbol{G}_H^{\theta}\right]_{11}^{(i)}\boldsymbol{L}'^{(i)}_{::1} + \left[\boldsymbol{G}_H^{\theta}\right]_{12}^{(i)}\boldsymbol{L}'^{(i)}_{::2} + \left[\boldsymbol{G}_H^{\theta}\right]_{13}^{(i)}\boldsymbol{L}'^{(i)}_{::3} + \left[\boldsymbol{G}_H^{\theta}\right]_{14}^{(i)}\boldsymbol{L}'^{(i)}_{::4} + \left[\boldsymbol{G}_H^{\theta}\right]_{15}^{(i)}\boldsymbol{L}'^{(i)}_{::5} + \left[\boldsymbol{G}_H^{\theta}\right]_{16}^{(i)}\boldsymbol{L}'^{(i)}_{::6} \\ \left[\boldsymbol{G}_H^{\theta}\right]_{21}^{(i)}\boldsymbol{L}'^{(i)}_{::1} + \left[\boldsymbol{G}_H^{\theta}\right]_{22}^{(i)}\boldsymbol{L}'^{(i)}_{::2} + \left[\boldsymbol{G}_H^{\theta}\right]_{23}^{(i)}\boldsymbol{L}'^{(i)}_{::3} + \left[\boldsymbol{G}_H^{\theta}\right]_{24}^{(i)}\boldsymbol{L}'^{(i)}_{::4} + \left[\boldsymbol{G}_H^{\theta}\right]_{25}^{(i)}\boldsymbol{L}'^{(i)}_{::5} + \left[\boldsymbol{G}_H^{\theta}\right]_{26}^{(i)}\boldsymbol{L}'^{(i)}_{::6} \\ \left[\boldsymbol{G}_H^{\theta}\right]_{31}^{(i)}\boldsymbol{L}'^{(i)}_{::1} + \left[\boldsymbol{G}_H^{\theta}\right]_{32}^{(i)}\boldsymbol{L}'^{(i)}_{::2} + \left[\boldsymbol{G}_H^{\theta}\right]_{33}^{(i)}\boldsymbol{L}'^{(i)}_{::3} + \left[\boldsymbol{G}_H^{\theta}\right]_{34}^{(i)}\boldsymbol{L}'^{(i)}_{::4} + \left[\boldsymbol{G}_H^{\theta}\right]_{35}^{(i)}\boldsymbol{L}'^{(i)}_{::5} + \left[\boldsymbol{G}_H^{\theta}\right]_{36}^{(i)}\boldsymbol{L}'^{(i)}_{::6} \\ \left[\boldsymbol{G}_H^{\theta}\right]_{41}^{(i)}\boldsymbol{L}'^{(i)}_{::1} + \left[\boldsymbol{G}_H^{\theta}\right]_{42}^{(i)}\boldsymbol{L}'^{(i)}_{::2} + \left[\boldsymbol{G}_H^{\theta}\right]_{43}^{(i)}\boldsymbol{L}'^{(i)}_{::3} + \left[\boldsymbol{G}_H^{\theta}\right]_{44}^{(i)}\boldsymbol{L}'^{(i)}_{::4} + \left[\boldsymbol{G}_H^{\theta}\right]_{45}^{(i)}\boldsymbol{L}'^{(i)}_{::5} + \left[\boldsymbol{G}_H^{\theta}\right]_{46}^{(i)}\boldsymbol{L}'^{(i)}_{::6} \\ \left[\boldsymbol{G}_H^{\theta}\right]_{51}^{(i)}\boldsymbol{L}'^{(i)}_{::1} + \left[\boldsymbol{G}_H^{\theta}\right]_{52}^{(i)}\boldsymbol{L}'^{(i)}_{::2} + \left[\boldsymbol{G}_H^{\theta}\right]_{53}^{(i)}\boldsymbol{L}'^{(i)}_{::3} + \left[\boldsymbol{G}_H^{\theta}\right]_{54}^{(i)}\boldsymbol{L}'^{(i)}_{::4} + \left[\boldsymbol{G}_H^{\theta}\right]_{55}^{(i)}\boldsymbol{L}'^{(i)}_{::5} + \left[\boldsymbol{G}_H^{\theta}\right]_{56}^{(i)}\boldsymbol{L}'^{(i)}_{::6} \\ \left[\boldsymbol{G}_H^{\theta}\right]_{61}^{(i)}\boldsymbol{L}'^{(i)}_{::1} + \left[\boldsymbol{G}_H^{\theta}\right]_{62}^{(i)}\boldsymbol{L}'^{(i)}_{::2} + \left[\boldsymbol{G}_H^{\theta}\right]_{63}^{(i)}\boldsymbol{L}'^{(i)}_{::3} + \left[\boldsymbol{G}_H^{\theta}\right]_{64}^{(i)}\boldsymbol{L}'^{(i)}_{::4} + \left[\boldsymbol{G}_H^{\theta}\right]_{65}^{(i)}\boldsymbol{L}'^{(i)}_{::5} + \left[\boldsymbol{G}_H^{\theta}\right]_{66}^{(i)}\boldsymbol{L}'^{(i)}_{::6} \end{bmatrix}$,

$$\boldsymbol{L}'^{(i)} = \begin{bmatrix} \left[\boldsymbol{G}_q^{\theta}\right]_{(i)}^{\mathrm{T}}[\boldsymbol{H}_{\theta}^{H}]_{::1}^{(i)}\left[\boldsymbol{G}_q^{\theta}\right]_{(i)} & \left[\boldsymbol{G}_q^{\theta}\right]_{(i)}^{\mathrm{T}}[\boldsymbol{H}_{\theta}^{H}]_{::2}^{(i)}\left[\boldsymbol{G}_q^{\theta}\right]_{(i)} & \left[\boldsymbol{G}_q^{\theta}\right]_{(i)}^{\mathrm{T}}[\boldsymbol{H}_{\theta}^{H}]_{::3}^{(i)}\left[\boldsymbol{G}_q^{\theta}\right]_{(i)} \\ \left[\boldsymbol{G}_q^{\theta}\right]_{(i)}^{\mathrm{T}}[\boldsymbol{H}_{\theta}^{H}]_{::4}^{(i)}\left[\boldsymbol{G}_q^{\theta}\right]_{(i)} & \left[\boldsymbol{G}_q^{\theta}\right]_{(i)}^{\mathrm{T}}[\boldsymbol{H}_{\theta}^{H}]_{::5}^{(i)}\left[\boldsymbol{G}_q^{\theta}\right]_{(i)} & \left[\boldsymbol{G}_q^{\theta}\right]_{(i)}^{\mathrm{T}}[\boldsymbol{H}_{\theta}^{H}]_{::6}^{(i)}\left[\boldsymbol{G}_q^{\theta}\right]_{(i)} \end{bmatrix}^{\mathrm{T}}.$$

Here, $\boldsymbol{L}'^{(i)}_{::i}$ denotes the i-th layer of the three-dimensional matrix $\boldsymbol{L}'^{(i)}$; $[\boldsymbol{H}_{\theta}^{H}]_{::i}^{(i)}$ represents the i-th layer of the three-dimensional matrix $\left[\boldsymbol{H}_{\theta}^{H}\right]^{(i)}$; $\left[\boldsymbol{G}_H^{\theta}\right]_{11}^{(i)}$ represents the elements of the first row and the first column of the matrix $\left[\boldsymbol{G}_H^{\theta}\right]^{(i)}$, and similarly hereinafter.

By isolating the acceleration corresponding to the actuated joint in Equation (21), the equation can be rewritten as

$$\ddot{\boldsymbol{\theta}}_3^{(i)} = \left[\boldsymbol{G}_H^{\theta}\right]_{3:}^{(i)}\boldsymbol{A}_H - \dot{\boldsymbol{q}}^{\mathrm{T}}\boldsymbol{L}_{::3}^{(i)}\dot{\boldsymbol{q}} \tag{22}$$

In Equation (22), $\ddot{\boldsymbol{\theta}}_3^{(i)}$ denotes the acceleration of the prismatic joint in the UPU branch chain i, while $\boldsymbol{L}_{::3}^{(i)}$ represents the third layer of the three-dimensional matrix $\boldsymbol{L}^{(i)}$ associated with the UPU branch chain $\underline{i}$.

By combining Equation (22) into a single expression, one obtains

$$\ddot{\boldsymbol{q}} = \boldsymbol{G}_H^{q}\boldsymbol{A}_H - \dot{\boldsymbol{q}}^{\mathrm{T}}\boldsymbol{H}_H^{q}\dot{\boldsymbol{q}} \tag{23}$$

where $\ddot{\boldsymbol{q}} = \begin{bmatrix}\ddot{\theta}_3^{(1)} & \ddot{\theta}_3^{(2)} & \ddot{\theta}_3^{(3)} & \ddot{\theta}_3^{(4)} & 0 & 0\end{bmatrix}^{\mathrm{T}}$, $\boldsymbol{H}_H^{q} = \begin{bmatrix}\boldsymbol{L}_{::3}^{(1)} & \boldsymbol{L}_{::3}^{(2)} & \boldsymbol{L}_{::3}^{(3)} & \boldsymbol{L}_{::3}^{(4)} & \boldsymbol{L}_{::6}^{(3)} & \boldsymbol{L}_{::6}^{(4)}\end{bmatrix}^{\mathrm{T}}$.

If the acceleration $\boldsymbol{A}_H$ of Foot I is expressed in terms of the second-order influence coefficients with respect to the generalized actuated joints, then Equation (23) can be written as

$$\boldsymbol{A}_H = \boldsymbol{G}_q^{H}\ddot{\boldsymbol{q}} + \dot{\boldsymbol{q}}^{\mathrm{T}}\boldsymbol{H}_q^{H}\dot{\boldsymbol{q}} \tag{24}$$

where $\boldsymbol{H}_q^H = \begin{bmatrix} \left[\boldsymbol{G}_q^H\right]_{11}\left[\boldsymbol{H}_H^q\right]_{::1} + \left[\boldsymbol{G}_q^H\right]_{12}\left[\boldsymbol{H}_H^q\right]_{::2} + \left[\boldsymbol{G}_q^H\right]_{13}\left[\boldsymbol{H}_H^q\right]_{::3} + \left[\boldsymbol{G}_q^H\right]_{14}\left[\boldsymbol{H}_H^q\right]_{::4} + \left[\boldsymbol{G}_q^H\right]_{15}\left[\boldsymbol{H}_H^q\right]_{::5} + \left[\boldsymbol{G}_q^H\right]_{16}\left[\boldsymbol{H}_H^q\right]_{::6} \\ \left[\boldsymbol{G}_q^H\right]_{21}\left[\boldsymbol{H}_H^q\right]_{::1} + \left[\boldsymbol{G}_q^H\right]_{22}\left[\boldsymbol{H}_H^q\right]_{::2} + \left[\boldsymbol{G}_q^H\right]_{23}\left[\boldsymbol{H}_H^q\right]_{::3} + \left[\boldsymbol{G}_q^H\right]_{24}\left[\boldsymbol{H}_H^q\right]_{::4} + \left[\boldsymbol{G}_q^H\right]_{25}\left[\boldsymbol{H}_H^q\right]_{::5} + \left[\boldsymbol{G}_q^H\right]_{26}\left[\boldsymbol{H}_H^q\right]_{::6} \\ \left[\boldsymbol{G}_q^H\right]_{31}\left[\boldsymbol{H}_H^q\right]_{::1} + \left[\boldsymbol{G}_q^H\right]_{32}\left[\boldsymbol{H}_H^q\right]_{::2} + \left[\boldsymbol{G}_q^H\right]_{33}\left[\boldsymbol{H}_H^q\right]_{::3} + \left[\boldsymbol{G}_q^H\right]_{34}\left[\boldsymbol{H}_H^q\right]_{::4} + \left[\boldsymbol{G}_q^H\right]_{35}\left[\boldsymbol{H}_H^q\right]_{::5} + \left[\boldsymbol{G}_q^H\right]_{36}\left[\boldsymbol{H}_H^q\right]_{::6} \\ \left[\boldsymbol{G}_q^H\right]_{41}\left[\boldsymbol{H}_H^q\right]_{::1} + \left[\boldsymbol{G}_q^H\right]_{42}\left[\boldsymbol{H}_H^q\right]_{::2} + \left[\boldsymbol{G}_q^H\right]_{43}\left[\boldsymbol{H}_H^q\right]_{::3} + \left[\boldsymbol{G}_q^H\right]_{44}\left[\boldsymbol{H}_H^q\right]_{::4} + \left[\boldsymbol{G}_q^H\right]_{45}\left[\boldsymbol{H}_H^q\right]_{::5} + \left[\boldsymbol{G}_q^H\right]_{46}\left[\boldsymbol{H}_H^q\right]_{::6} \\ \left[\boldsymbol{G}_q^H\right]_{51}\left[\boldsymbol{H}_H^q\right]_{::1} + \left[\boldsymbol{G}_q^H\right]_{52}\left[\boldsymbol{H}_H^q\right]_{::2} + \left[\boldsymbol{G}_q^H\right]_{53}\left[\boldsymbol{H}_H^q\right]_{::3} + \left[\boldsymbol{G}_q^H\right]_{54}\left[\boldsymbol{H}_H^q\right]_{::4} + \left[\boldsymbol{G}_q^H\right]_{55}\left[\boldsymbol{H}_H^q\right]_{::5} + \left[\boldsymbol{G}_q^H\right]_{56}\left[\boldsymbol{H}_H^q\right]_{::6} \\ \left[\boldsymbol{G}_q^H\right]_{61}\left[\boldsymbol{H}_H^q\right]_{::1} + \left[\boldsymbol{G}_q^H\right]_{62}\left[\boldsymbol{H}_H^q\right]_{::2} + \left[\boldsymbol{G}_q^H\right]_{63}\left[\boldsymbol{H}_H^q\right]_{::3} + \left[\boldsymbol{G}_q^H\right]_{64}\left[\boldsymbol{H}_H^q\right]_{::4} + \left[\boldsymbol{G}_q^H\right]_{65}\left[\boldsymbol{H}_H^q\right]_{::5} + \left[\boldsymbol{G}_q^H\right]_{66}\left[\boldsymbol{H}_H^q\right]_{::6} \end{bmatrix}$, which represents the second-order kinematic influence coefficient matrix of the dual-platform biped robot, namely the Hessian matrix. Here, $\left[\boldsymbol{H}_H^q\right]_{::i}$ represents the i-th layer of the three-dimensional matrix $\boldsymbol{H}_H^q$.

By substituting Equation (24) into Equation (21) and simplifying, the following expression is obtained:

$$\ddot{\boldsymbol{\theta}}^{(i)} = \left[\boldsymbol{G}_H^\theta\right]^{(i)}\left(\boldsymbol{G}_q^H\ddot{\boldsymbol{q}} + \dot{\boldsymbol{q}}^{\mathrm{T}}\boldsymbol{H}_q^H\dot{\boldsymbol{q}}\right) - \dot{\boldsymbol{q}}^{\mathrm{T}}\boldsymbol{L}^{(i)}\dot{\boldsymbol{q}} = \dot{\boldsymbol{q}}^{\mathrm{T}}\left[\boldsymbol{H}_q^\theta\right]^{(i)}\dot{\boldsymbol{q}} + \left[\boldsymbol{G}_q^\theta\right]^{(i)}\ddot{\boldsymbol{q}} \tag{25}$$

In this expression,

$$[\boldsymbol{H}_q^\theta]^{(i)} = \begin{bmatrix} \left[\boldsymbol{G}_H^\theta\right]_{11}^{(i)}\left[\boldsymbol{H}_q^H\right]_{::1} + \left[\boldsymbol{G}_H^\theta\right]_{12}^{(i)}\left[\boldsymbol{H}_q^H\right]_{::2} + \left[\boldsymbol{G}_H^\theta\right]_{13}^{(i)}\left[\boldsymbol{H}_q^H\right]_{::3} + \left[\boldsymbol{G}_H^\theta\right]_{14}^{(i)}\left[\boldsymbol{H}_q^H\right]_{::4} + \left[\boldsymbol{G}_H^\theta\right]_{15}^{(i)}\left[\boldsymbol{H}_q^H\right]_{::5} + \left[\boldsymbol{G}_H^\theta\right]_{16}^{(i)}\left[\boldsymbol{H}_q^H\right]_{::6} \\ \left[\boldsymbol{G}_H^\theta\right]_{21}^{(i)}\left[\boldsymbol{H}_q^H\right]_{::1} + \left[\boldsymbol{G}_H^\theta\right]_{22}^{(i)}\left[\boldsymbol{H}_q^H\right]_{::2} + \left[\boldsymbol{G}_H^\theta\right]_{23}^{(i)}\left[\boldsymbol{H}_q^H\right]_{::3} + \left[\boldsymbol{G}_H^\theta\right]_{24}^{(i)}\left[\boldsymbol{H}_q^H\right]_{::4} + \left[\boldsymbol{G}_H^\theta\right]_{25}^{(i)}\left[\boldsymbol{H}_q^H\right]_{::5} + \left[\boldsymbol{G}_H^\theta\right]_{26}^{(i)}\left[\boldsymbol{H}_q^H\right]_{::6} \\ \left[\boldsymbol{G}_H^\theta\right]_{31}^{(i)}\left[\boldsymbol{H}_q^H\right]_{::1} + \left[\boldsymbol{G}_H^\theta\right]_{32}^{(i)}\left[\boldsymbol{H}_q^H\right]_{::2} + \left[\boldsymbol{G}_H^\theta\right]_{33}^{(i)}\left[\boldsymbol{H}_q^H\right]_{::3} + \left[\boldsymbol{G}_H^\theta\right]_{34}^{(i)}\left[\boldsymbol{H}_q^H\right]_{::4} + \left[\boldsymbol{G}_H^\theta\right]_{35}^{(i)}\left[\boldsymbol{H}_q^H\right]_{::5} + \left[\boldsymbol{G}_H^\theta\right]_{36}^{(i)}\left[\boldsymbol{H}_q^H\right]_{::6} \\ \left[\boldsymbol{G}_H^\theta\right]_{41}^{(i)}\left[\boldsymbol{H}_q^H\right]_{::1} + \left[\boldsymbol{G}_H^\theta\right]_{42}^{(i)}\left[\boldsymbol{H}_q^H\right]_{::2} + \left[\boldsymbol{G}_H^\theta\right]_{43}^{(i)}\left[\boldsymbol{H}_q^H\right]_{::3} + \left[\boldsymbol{G}_H^\theta\right]_{44}^{(i)}\left[\boldsymbol{H}_q^H\right]_{::4} + \left[\boldsymbol{G}_H^\theta\right]_{45}^{(i)}\left[\boldsymbol{H}_q^H\right]_{::5} + \left[\boldsymbol{G}_H^\theta\right]_{46}^{(i)}\left[\boldsymbol{H}_q^H\right]_{::6} \\ \left[\boldsymbol{G}_H^\theta\right]_{51}^{(i)}\left[\boldsymbol{H}_q^H\right]_{::1} + \left[\boldsymbol{G}_H^\theta\right]_{52}^{(i)}\left[\boldsymbol{H}_q^H\right]_{::2} + \left[\boldsymbol{G}_H^\theta\right]_{53}^{(i)}\left[\boldsymbol{H}_q^H\right]_{::3} + \left[\boldsymbol{G}_H^\theta\right]_{54}^{(i)}\left[\boldsymbol{H}_q^H\right]_{::4} + \left[\boldsymbol{G}_H^\theta\right]_{55}^{(i)}\left[\boldsymbol{H}_q^H\right]_{::5} + \left[\boldsymbol{G}_H^\theta\right]_{56}^{(i)}\left[\boldsymbol{H}_q^H\right]_{::6} \\ \left[\boldsymbol{G}_H^\theta\right]_{61}^{(i)}\left[\boldsymbol{H}_q^H\right]_{::1} + \left[\boldsymbol{G}_H^\theta\right]_{62}^{(i)}\left[\boldsymbol{H}_q^H\right]_{::2} + \left[\boldsymbol{G}_H^\theta\right]_{63}^{(i)}\left[\boldsymbol{H}_q^H\right]_{::3} + \left[\boldsymbol{G}_H^\theta\right]_{64}^{(i)}\left[\boldsymbol{H}_q^H\right]_{::4} + \left[\boldsymbol{G}_H^\theta\right]_{65}^{(i)}\left[\boldsymbol{H}_q^H\right]_{::5} + \left[\boldsymbol{G}_H^\theta\right]_{66}^{(i)}\left[\boldsymbol{H}_q^H\right]_{::6} \end{bmatrix} - \boldsymbol{L}^{(i)}.$$

Here, $\left[\boldsymbol{H}_q^H\right]_{::i}^{(i)}$ denotes the i-th layer of the three-dimensional matrix $\left[\boldsymbol{H}_q^H\right]^{(i)}$, and similarly hereinafter.

By differentiating both sides of Equation (15) with respect to time, the CoM acceleration $\boldsymbol{A}_{k1}^{(i)}$ of the swinging link k_1 in the UPU branch chain i can be derived as

$$\boldsymbol{A}_{k1}^{(i)} = \left[\boldsymbol{G}_\theta^{k1}\right]^{(i)}\ddot{\boldsymbol{\theta}}_{k1}^{(i)} + \left[\dot{\boldsymbol{\theta}}_{k1}^{(i)}\right]^{\mathrm{T}}\left[\boldsymbol{H}_\theta^{k1}\right]^{(i)}\dot{\boldsymbol{\theta}}_{k1}^{(i)} \tag{26}$$

Here, $\boldsymbol{A}_{k1}^{(i)} = \begin{bmatrix}\varepsilon_{k1x} & \varepsilon_{k1y} & \varepsilon_{k1z} & a_{k1x} & a_{k1y} & a_{k1z}\end{bmatrix}^{\mathrm{T}}$, $\left[\boldsymbol{H}_\theta^{k1}\right]^{(i)}$ is a 2×2 six-dimensional column vector.

The first and second rows of matrix $\left[\boldsymbol{H}_\theta^{k1}\right]^{(i)}$ are given respectively as

$$\left[\boldsymbol{H}_\theta^{k1}\right]_{1::}^{(i)} = \begin{bmatrix} \boldsymbol{0} & \boldsymbol{S}_{i1} \times \boldsymbol{S}_{i2} \\ \boldsymbol{S}_{i1} \times [\boldsymbol{S}_{i1} \times (\boldsymbol{P}_{k1}^{(i)} - \boldsymbol{A}_i)] & \boldsymbol{S}_{i1} \times [\boldsymbol{S}_{i2} \times (\boldsymbol{P}_{k1}^{(i)} - \boldsymbol{A}_i)] \end{bmatrix}; \left[\boldsymbol{H}_\theta^{k1}\right]_{2::}^{(i)} = \begin{bmatrix} \boldsymbol{0} & \boldsymbol{0} \\ \boldsymbol{S}_{i1} \times [\boldsymbol{S}_{i2} \times (\boldsymbol{P}_{k1}^{(i)} - \boldsymbol{A}_i)] & \boldsymbol{S}_{i2} \times [\boldsymbol{S}_{i2} \times (\boldsymbol{P}_{k1}^{(i)} - \boldsymbol{A}_i)] \end{bmatrix} \tag{27}$$

Here, $\left[\boldsymbol{H}_\theta^{k1}\right]_{i::}^{(i)}$ denotes the i-th row of the three-dimensional matrix $\left[\boldsymbol{H}_\theta^{k1}\right]^{(i)}$, and similarly hereinafter.

By combining Equations (21), (25), and (26) and rearranging, the acceleration mapping between the swinging link k_1 and the generalized actuated joints can be expressed as

$$\boldsymbol{A}_{k1}^{(i)} = \dot{\boldsymbol{q}}^{\mathrm{T}}\left[\boldsymbol{H}_q^{k1}\right]^{(i)}\dot{\boldsymbol{q}} + \left[\boldsymbol{G}_q^{k1}\right]^{(i)}\ddot{\boldsymbol{q}} \tag{28}$$

where $\left[\boldsymbol{H}_q^{k1}\right]^{(i)} = \boldsymbol{M}_{k1}^{(i)} + \boldsymbol{N}_{k1}^{(i)}$.

$$\text{Here, } \boldsymbol{M}_{k1}^{(i)} = \begin{bmatrix} \left[\boldsymbol{G}_{\theta}^{k1}\right]_{11}^{(i)} \left[\boldsymbol{H}_{q}^{\theta}\right]_{::1}^{(i)} + \left[\boldsymbol{G}_{\theta}^{k1}\right]_{12}^{(i)} \left[\boldsymbol{H}_{q}^{\theta}\right]_{::2}^{(i)} \\ \left[\boldsymbol{G}_{\theta}^{k1}\right]_{21}^{(i)} \left[\boldsymbol{H}_{q}^{\theta}\right]_{::1}^{(i)} + \left[\boldsymbol{G}_{\theta}^{k1}\right]_{22}^{(i)} \left[\boldsymbol{H}_{q}^{\theta}\right]_{::2}^{(i)} \\ \left[\boldsymbol{G}_{\theta}^{k1}\right]_{31}^{(i)} \left[\boldsymbol{H}_{q}^{\theta}\right]_{::1}^{(i)} + \left[\boldsymbol{G}_{\theta}^{k1}\right]_{32}^{(i)} \left[\boldsymbol{H}_{q}^{\theta}\right]_{::2}^{(i)} \\ \left[\boldsymbol{G}_{\theta}^{k1}\right]_{41}^{(i)} \left[\boldsymbol{H}_{q}^{\theta}\right]_{::1}^{(i)} + \left[\boldsymbol{G}_{\theta}^{k1}\right]_{42}^{(i)} \left[\boldsymbol{H}_{q}^{\theta}\right]_{::2}^{(i)} \\ \left[\boldsymbol{G}_{\theta}^{k1}\right]_{51}^{(i)} \left[\boldsymbol{H}_{q}^{\theta}\right]_{::1}^{(i)} + \left[\boldsymbol{G}_{\theta}^{k1}\right]_{52}^{(i)} \left[\boldsymbol{H}_{q}^{\theta}\right]_{::2}^{(i)} \\ \left[\boldsymbol{G}_{\theta}^{k1}\right]_{61}^{(i)} \left[\boldsymbol{H}_{q}^{\theta}\right]_{::1}^{(i)} + \left[\boldsymbol{G}_{\theta}^{k1}\right]_{62}^{(i)} \left[\boldsymbol{H}_{q}^{\theta}\right]_{::2}^{(i)} \end{bmatrix}; \boldsymbol{N}_{k1}^{(i)} = \begin{bmatrix} \left[\left[\boldsymbol{G}_{q}^{\theta}\right]_{1:,2:}^{(i)}\right]^{\mathrm{T}} \left[\boldsymbol{H}_{\theta}^{k1}\right]_{::1}^{(i)} \left[\boldsymbol{G}_{q}^{\theta}\right]_{1:,2:}^{(i)} \\ \left[\left[\boldsymbol{G}_{q}^{\theta}\right]_{1:,2:}^{(i)}\right]^{\mathrm{T}} \left[\boldsymbol{H}_{\theta}^{k1}\right]_{::2}^{(i)} \left[\boldsymbol{G}_{q}^{\theta}\right]_{1:,2:}^{(i)} \\ \left[\left[\boldsymbol{G}_{q}^{\theta}\right]_{1:,2:}^{(i)}\right]^{\mathrm{T}} \left[\boldsymbol{H}_{\theta}^{k1}\right]_{::3}^{(i)} \left[\boldsymbol{G}_{q}^{\theta}\right]_{1:,2:}^{(i)} \\ \left[\left[\boldsymbol{G}_{q}^{\theta}\right]_{1:,2:}^{(i)}\right]^{\mathrm{T}} \left[\boldsymbol{H}_{\theta}^{k1}\right]_{::4}^{(i)} \left[\boldsymbol{G}_{q}^{\theta}\right]_{1:,2:}^{(i)} \\ \left[\left[\boldsymbol{G}_{q}^{\theta}\right]_{1:,2:}^{(i)}\right]^{\mathrm{T}} \left[\boldsymbol{H}_{\theta}^{k1}\right]_{::5}^{(i)} \left[\boldsymbol{G}_{q}^{\theta}\right]_{1:,2:}^{(i)} \\ \left[\left[\boldsymbol{G}_{q}^{\theta}\right]_{1:,2:}^{(i)}\right]^{\mathrm{T}} \left[\boldsymbol{H}_{\theta}^{k1}\right]_{::6}^{(i)} \left[\boldsymbol{G}_{q}^{\theta}\right]_{1:,2:}^{(i)} \end{bmatrix}.$$

Let the CoM acceleration of the telescopic link k_2 be denoted as $\boldsymbol{A}_{k2}$. By differentiating both sides of Equation (17) with respect to time, one obtains

$$\boldsymbol{A}_{k2}^{(i)} = \left[\boldsymbol{G}_{\theta}^{k2}\right]^{(i)} \ddot{\boldsymbol{\theta}}_{k2}^{(i)} + \left[\dot{\boldsymbol{\theta}}_{k2}^{(i)}\right]^{\mathrm{T}} \left[\boldsymbol{H}_{\theta}^{k2}\right]^{(i)} \dot{\boldsymbol{\theta}}_{k2}^{(i)} \tag{29}$$

where $\boldsymbol{A}_{k2}^{(i)} = \begin{bmatrix} \varepsilon_{k2x} & \varepsilon_{k2y} & \varepsilon_{k2z} & a_{k2x} & a_{k2y} & a_{k2z} \end{bmatrix}^{\mathrm{T}}$, $\left[\boldsymbol{H}_{\theta}^{k2}\right]^{(i)}$ is a 3×3 six-dimensional column vector.

Accordingly, the three rows of the matrix $\left[\boldsymbol{H}_{\theta}^{k2}\right]^{(i)}$ are given, respectively, as

$$\left[\boldsymbol{H}_{\theta}^{k2}\right]_{1::}^{(i)} = \begin{bmatrix} \begin{bmatrix} \boldsymbol{0} \\ \boldsymbol{S}_{i1} \times [\boldsymbol{S}_{i1} \times (\boldsymbol{P}_{k2}^{(i)} - \boldsymbol{A}_i)] \end{bmatrix} \\ \begin{bmatrix} \boldsymbol{S}_{i1} \times \boldsymbol{S}_{i2} \\ \boldsymbol{S}_{i1} \times [\boldsymbol{S}_{i2} \times (\boldsymbol{P}_{k2}^{(i)} - \boldsymbol{A}_i)] \end{bmatrix} \\ \begin{bmatrix} \boldsymbol{0} \\ \boldsymbol{S}_{i1} \times \boldsymbol{S}_{i3} \end{bmatrix} \end{bmatrix}^{\mathrm{T}}; \left[\boldsymbol{H}_{\theta}^{k2}\right]_{2::}^{(i)} = \begin{bmatrix} \begin{bmatrix} \boldsymbol{0} \\ \boldsymbol{S}_{i1} \times [\boldsymbol{S}_{i2} \times (\boldsymbol{P}_{k2}^{(i)} - \boldsymbol{A}_i)] \end{bmatrix} \\ \begin{bmatrix} \boldsymbol{0} \\ \boldsymbol{S}_{i2} \times [\boldsymbol{S}_{i2} \times (\boldsymbol{P}_{k2}^{(i)} - \boldsymbol{A}_i)] \end{bmatrix} \\ \begin{bmatrix} \boldsymbol{0} \\ \boldsymbol{S}_{i2} \times \boldsymbol{S}_{i3} \end{bmatrix} \end{bmatrix}^{\mathrm{T}}; \left[\boldsymbol{H}_{\theta}^{k2}\right]_{3::}^{(i)} = \begin{bmatrix} \begin{bmatrix} \boldsymbol{0} \\ \boldsymbol{S}_{i1} \times \boldsymbol{S}_{i3} \end{bmatrix} \\ \begin{bmatrix} \boldsymbol{0} \\ \boldsymbol{S}_{i2} \times \boldsymbol{S}_{i3} \end{bmatrix} \\ \begin{bmatrix} \boldsymbol{0} \\ \boldsymbol{0} \end{bmatrix} \end{bmatrix}^{\mathrm{T}} \tag{30}$$

Similarly, the acceleration mapping between the telescopic link k_2 and the generalized actuated joints can be expressed as

$$\boldsymbol{A}_{k2}^{(i)} = \dot{\boldsymbol{q}}^{\mathrm{T}} \left[\boldsymbol{H}_{\theta}^{k2}\right]^{(i)} \dot{\boldsymbol{q}} + \left[\boldsymbol{G}_{q}^{k2}\right]^{(i)} \ddot{\boldsymbol{q}} \tag{31}$$

where $\left[\boldsymbol{H}_{q}^{k2}\right]^{(i)} = \boldsymbol{M}_{k2}^{(i)} + \boldsymbol{N}_{k2}^{(i)}$.

$$\text{Here, } \boldsymbol{M}_{k2}^{(i)} = \begin{bmatrix} \left[\boldsymbol{G}_{\theta}^{k1}\right]_{11}^{(i)} \left[\boldsymbol{H}_{q}^{\theta}\right]_{::1}^{(i)} + \left[\boldsymbol{G}_{\theta}^{k1}\right]_{12}^{(i)} \left[\boldsymbol{H}_{q}^{\theta}\right]_{::2}^{(i)} + \left[\boldsymbol{G}_{\theta}^{k2}\right]_{13}^{(i)} \left[\boldsymbol{H}_{q}^{\theta}\right]_{::3}^{(i)} \\ \left[\boldsymbol{G}_{\theta}^{k1}\right]_{21}^{(i)} \left[\boldsymbol{H}_{q}^{\theta}\right]_{::1}^{(i)} + \left[\boldsymbol{G}_{\theta}^{k1}\right]_{22}^{(i)} \left[\boldsymbol{H}_{q}^{\theta}\right]_{::2}^{(i)} + \left[\boldsymbol{G}_{\theta}^{k2}\right]_{23}^{(i)} \left[\boldsymbol{H}_{q}^{\theta}\right]_{::3}^{(i)} \\ \left[\boldsymbol{G}_{\theta}^{k1}\right]_{31}^{(i)} \left[\boldsymbol{H}_{q}^{\theta}\right]_{::1}^{(i)} + \left[\boldsymbol{G}_{\theta}^{k1}\right]_{32}^{(i)} \left[\boldsymbol{H}_{q}^{\theta}\right]_{::2}^{(i)} + \left[\boldsymbol{G}_{\theta}^{k2}\right]_{33}^{(i)} \left[\boldsymbol{H}_{q}^{\theta}\right]_{::3}^{(i)} \\ \left[\boldsymbol{G}_{\theta}^{k1}\right]_{41}^{(i)} \left[\boldsymbol{H}_{q}^{\theta}\right]_{::1}^{(i)} + \left[\boldsymbol{G}_{\theta}^{k1}\right]_{42}^{(i)} \left[\boldsymbol{H}_{q}^{\theta}\right]_{::2}^{(i)} + \left[\boldsymbol{G}_{\theta}^{k2}\right]_{43}^{(i)} \left[\boldsymbol{H}_{q}^{\theta}\right]_{::3}^{(i)} \\ \left[\boldsymbol{G}_{\theta}^{k1}\right]_{51}^{(i)} \left[\boldsymbol{H}_{q}^{\theta}\right]_{::1}^{(i)} + \left[\boldsymbol{G}_{\theta}^{k1}\right]_{52}^{(i)} \left[\boldsymbol{H}_{q}^{\theta}\right]_{::2}^{(i)} + \left[\boldsymbol{G}_{\theta}^{k2}\right]_{53}^{(i)} \left[\boldsymbol{H}_{q}^{\theta}\right]_{::3}^{(i)} \\ \left[\boldsymbol{G}_{\theta}^{k1}\right]_{61}^{(i)} \left[\boldsymbol{H}_{q}^{\theta}\right]_{::1}^{(i)} + \left[\boldsymbol{G}_{\theta}^{k1}\right]_{62}^{(i)} \left[\boldsymbol{H}_{q}^{\theta}\right]_{::2}^{(i)} + \left[\boldsymbol{G}_{\theta}^{k2}\right]_{63}^{(i)} \left[\boldsymbol{H}_{q}^{\theta}\right]_{::3}^{(i)} \end{bmatrix};$$

$$\boldsymbol{N}_{k2}^{(i)} = \begin{bmatrix} \left[\left[\boldsymbol{G}_{q}^{\theta}\right]_{1:,2:,3:}^{(i)}\right]^{\mathrm{T}} \left[\boldsymbol{H}_{\theta}^{k2}\right]_{::1}^{(i)} \left[\boldsymbol{G}_{q}^{\theta}\right]_{1:,2:,3:}^{(i)} \\ \left[\left[\boldsymbol{G}_{q}^{\theta}\right]_{1:,2:,3:}^{(i)}\right]^{\mathrm{T}} \left[\boldsymbol{H}_{\theta}^{k2}\right]_{::2}^{(i)} \left[\boldsymbol{G}_{q}^{\theta}\right]_{1:,2:,3:}^{(i)} \\ \left[\left[\boldsymbol{G}_{q}^{\theta}\right]_{1:,2:,3:}^{(i)}\right]^{\mathrm{T}} \left[\boldsymbol{H}_{\theta}^{k2}\right]_{::3}^{(i)} \left[\boldsymbol{G}_{q}^{\theta}\right]_{1:,2:,3:}^{(i)} \\ \left[\left[\boldsymbol{G}_{q}^{\theta}\right]_{1:,2:,3:}^{(i)}\right]^{\mathrm{T}} \left[\boldsymbol{H}_{\theta}^{k2}\right]_{::4}^{(i)} \left[\boldsymbol{G}_{q}^{\theta}\right]_{1:,2:,3:}^{(i)} \\ \left[\left[\boldsymbol{G}_{q}^{\theta}\right]_{1:,2:,3:}^{(i)}\right]^{\mathrm{T}} \left[\boldsymbol{H}_{\theta}^{k2}\right]_{::5}^{(i)} \left[\boldsymbol{G}_{q}^{\theta}\right]_{1:,2:,3:}^{(i)} \\ \left[\left[\boldsymbol{G}_{q}^{\theta}\right]_{1:,2:,3:}^{(i)}\right]^{\mathrm{T}} \left[\boldsymbol{H}_{\theta}^{k2}\right]_{::6}^{(i)} \left[\boldsymbol{G}_{q}^{\theta}\right]_{1:,2:,3:}^{(i)} \end{bmatrix}.$$

3. Dynamics Model of the Biped Robot

3.1. Force Analysis

This section presents the dynamic modeling of the dual-platform biped robot, starting with the force analysis of the moving platform. In the biped robot, the resultant force and resultant torque acting on the moving platform are given respectively as the following expressions:

$$\boldsymbol{F}_H = \begin{bmatrix} \boldsymbol{n}_E - \boldsymbol{R}\boldsymbol{I}_c\boldsymbol{R}^{\mathrm{T}}\boldsymbol{\varepsilon}_H - \boldsymbol{\omega}_H \times \left[\boldsymbol{R}\boldsymbol{I}_c\boldsymbol{R}^{\mathrm{T}}\boldsymbol{\omega}_H\right] \\ m_H(\boldsymbol{g} - \boldsymbol{a}_H) + \boldsymbol{f}_E \end{bmatrix} \tag{32}$$

where m_H denotes the mass of the moving platform, $\boldsymbol{I}_c$ represents its moment of inertia with respect to the moving coordinate system $\{O_3\}$, $\boldsymbol{g}$ = [0, 0, −9806.65] $^{\mathrm{T}}$ mm/s^2 is the gravitational acceleration, and $\boldsymbol{f}_E$ and $\boldsymbol{n}_E$ denote the external force and external torque acting on the moving platform, respectively. Since external forces and torques are not considered in this paper, both $\boldsymbol{f}_E$ and $\boldsymbol{n}_E$ are set to zero.

Beyond the moving platform, the force analysis of the branch links is considered. To simplify the force analysis of the links, it is assumed that the motor mass is uniformly distributed within each link. As shown in Figure 4, local coordinate systems $\{o_{k1}\}$ and $\{o_{k2}\}$ are established at the CoM of the swinging link k_1 and the telescopic link k_2 of each branch, respectively. The rotation transformation matrices of the local coordinate systems $\{o_{k1}\}$ and $\{o_{k2}\}$ with respect to the fixed coordinate system $\{O_4\}$ can be expressed as

$$\begin{aligned} \left[\boldsymbol{R}_{k1}^{O_4}\right]^{(i)} &= \begin{bmatrix} \boldsymbol{S}_{i3} & \boldsymbol{S}_{i2} & \boldsymbol{S}_{i3} \times \boldsymbol{S}_{i2}/|\boldsymbol{S}_{i3} \times \boldsymbol{S}_{i2}| \end{bmatrix} \\ \left[\boldsymbol{R}_{k2}^{O_4}\right]^{(i)} &= \begin{bmatrix} \boldsymbol{S}_{i3} & \boldsymbol{S}_{i2} \times \boldsymbol{S}_{i3}/|\boldsymbol{S}_{i2} \times \boldsymbol{S}_{i3}| & \boldsymbol{S}_{i2} \end{bmatrix} \end{aligned} \tag{33}$$

Similarly, under the assumption that external forces and torques are neglected, a force analysis is carried out for the links in the UPU branch chain i. Since the swinging link k_1 and the telescopic link k_2 differ in their motion patterns and force characteristics, they must be analyzed separately. Accordingly, the resultant forces and resultant torques acting on the swinging link k_1 and the telescopic link k_2 are given, respectively, as

$$\begin{aligned} \boldsymbol{F}_{k1}^{(i)} &= \begin{bmatrix} -\left[\boldsymbol{R}_{k1}^{O_4}\right]^{(i)}\boldsymbol{I}_{k1}^{(i)}\left[\boldsymbol{R}_{k1}^{O_4}\right]_{(i)}^{\mathrm{T}}\boldsymbol{\varepsilon}_{k1}^{(i)} - \boldsymbol{\omega}_{k1}^{(i)} \times \left[\left[\boldsymbol{R}_{k1}^{O_4}\right]^{(i)}\boldsymbol{I}_{k1}^{(i)}\left[\boldsymbol{R}_{k1}^{O_4}\right]_{(i)}^{\mathrm{T}}\boldsymbol{\omega}_{k1}^{(i)}\right] \\ m_{k1}^{(i)}(\boldsymbol{g} - \boldsymbol{a}_{k1}^{(i)}) \end{bmatrix} \\ \boldsymbol{F}_{k2}^{(i)} &= \begin{bmatrix} -\left[\boldsymbol{R}_{k2}^{O_4}\right]^{(i)}\boldsymbol{I}_{k2}^{(i)}\left[\boldsymbol{R}_{k2}^{O_4}\right]_{(i)}^{\mathrm{T}}\boldsymbol{\varepsilon}_{k2}^{(i)} - \boldsymbol{\omega}_{k2}^{(i)} \times \left[\left[\boldsymbol{R}_{k2}^{O_4}\right]^{(i)}\boldsymbol{I}_{k2}^{(i)}\left[\boldsymbol{R}_{k2}^{O_4}\right]_{(i)}^{\mathrm{T}}\boldsymbol{\omega}_{k2}^{(i)}\right] \\ m_{k2}^{(i)}(\boldsymbol{g} - \boldsymbol{a}_{k2}^{(i)}) \end{bmatrix} \end{aligned} \tag{34}$$

where $m_{k1}^{(i)}$ and $m_{k2}^{(i)}$ denote the masses of the swinging link k_1 and telescopic link k_2 of the UPU branch chain i, respectively, while $\boldsymbol{I}_{k1}^{(i)}$ and $\boldsymbol{I}_{k2}^{(i)}$ represent their moments of inertia with respect to the local coordinate systems $\{o_{k1}\}$ and $\{o_{k2}\}$.

3.2. Dynamics Analysis

In the fixed coordinate system $\{O_4\}$, the forces and torques acting on each component can be equivalently simplified into a six-dimensional force vector applied at its CoM. This six-dimensional vector is then mapped into the equivalent driving forces at the four actuated joints through the force Jacobian matrix. Based on the above force transmission

relationship, the six-dimensional force vector acting on the moving platform can be transformed into the four actuated joints, and its equivalent driving forces can be expressed as

$$\boldsymbol{F}_{EH} = \left[\boldsymbol{G}_q^H\right]^{\mathrm{T}} \boldsymbol{F}_H = \left[\boldsymbol{G}_q^H\right]^{\mathrm{T}} \begin{bmatrix} \boldsymbol{n}_H \\ \boldsymbol{f}_H \end{bmatrix} \tag{35}$$



(**a**) (**b**)

Figure 4. Schematic diagram of the local coordinate systems of the links: (**a**) Swing link k_1 and (**b**) Expansion link k_2.

Specifically, the equivalent driving forces of the swinging link k_1 and the telescopic link k_2 in the UPU branch chain i with respect to the four actuated joints are given, respectively, as

$$\begin{aligned} \boldsymbol{F}_{Ek1}^{(i)} &= \left[\boldsymbol{G}_q^{k1}\right]_{(i)}^{\mathrm{T}} \boldsymbol{F}_{k1}^{(i)} = \left[\boldsymbol{G}_q^{k1}\right]_{(i)}^{\mathrm{T}} \begin{bmatrix} \boldsymbol{n}_{k1}^{(i)} \\ \boldsymbol{f}_{k1}^{(i)} \end{bmatrix} \\ \boldsymbol{F}_{Ek2}^{(i)} &= \left[\boldsymbol{G}_q^{k2}\right]_{(i)}^{\mathrm{T}} \boldsymbol{F}_{k2}^{(i)} = \left[\boldsymbol{G}_q^{k2}\right]_{(i)}^{\mathrm{T}} \begin{bmatrix} \boldsymbol{n}_{k2}^{(i)} \\ \boldsymbol{f}_{k2}^{(i)} \end{bmatrix} \end{aligned} \tag{36}$$

To simplify and focus on the robot's rigid body dynamics model, all joint actuators are assumed to be ideal power sources [31]. Based on the above force mapping, and according to the principle of virtual work, when joint friction is neglected, the sum of the virtual work performed by the driving forces, inertial forces, and external forces of the dual-platform biped robot is equal to zero. At this point, the system is in equilibrium, and the corresponding dynamic equations can be established as

$$\boldsymbol{\tau} + \boldsymbol{F}_{EB} + \sum_{i=1}^{4} \boldsymbol{F}_{Ek1}^{(i)} + \sum_{i=1}^{4} \boldsymbol{F}_{Ek2}^{(i)} = 0 \tag{37}$$

From Equation (37), the expression of the generalized actuating force of the dual-platform biped robot can be written as

$$\boldsymbol{\tau} = -\boldsymbol{F}_{EB} - \sum_{i=1}^{4} \boldsymbol{F}_{Ek1}^{(i)} - \sum_{i=1}^{4} \boldsymbol{F}_{Ek2}^{(i)} \tag{38}$$

where $\boldsymbol{\tau} = \begin{bmatrix} f_1 & f_2 & f_3 & f_4 & 0 & 0 \end{bmatrix}^{\mathrm{T}}$ denotes the driving forces of the four actuated joints of the biped robot.

Therefore, Equation (38) represents the dynamics model of the biped robot. Given the mass properties of the robot and the motion expressions of the moving platform, the magnitudes of the driving forces at the four actuated joints can be computed from Equation (38).

3.3. Numerical Verification

Building upon the dynamics analysis, it is necessary to further carry out numerical verification of the proposed model to ensure its reliability and accuracy. The velocity, acceleration, and driving force of the four actuated joints are comparatively validated through simulation results and theoretical calculations, based on the velocity and acceleration equations derived in the kinematic analysis in Section 2.

Referring to the structural schematic of the dual-platform biped robot shown in Figure 3, the basic structural parameters are given as a = 100 mm, b = 45 mm, c = 28 mm, d = 40 mm, h_1 = 200 mm, and h_2 = 160 mm. The mass properties of the dual-platform biped robot are provided in Table 2.

Table 2. Mass properties table for the dual-platform biped robot.

Component	Mass/g	CoM/mm	Moment of Inertia/g·mm^{-2}
Moving platform	1024	$(X, Y + 0.56\text{b} + 0.19\text{c}, 0.4Z + 0.6h_2)^{\mathrm{T}}$	diag (812,642, 5,395,508, 5,432,171)
Telescopic link $k_1^{(1)}$	8.9	$A_1 + 40(B_1 - A_1)/\mathrm{norm}(B_1 - A_1)$	diag (60, 5487, 5490)
Swinging link $k_2^{(1)}$	669.8	$B_1 + 40(A_1 - B_1)/\mathrm{norm}(A_1 - B_1)$	diag (358,957, 871,888, 888,886)
Telescopic link $k_1^{(2)}$	8.9	$A_2 + 40(B_2 - A_2)/\mathrm{norm}(B_2 - A_2)$	diag (60, 5487, 5490)
Swinging link $k_2^{(2)}$	669.8	$B_2 + 40(A_2 - B_2)/\mathrm{norm}(A_2 - B_2)$	diag (358,957, 871,888, 888,886)
Swinging link $k_1^{(3)}$	674.3	$A_3 + 57.5(B_3 - A_3)/\mathrm{norm}(B_3 - A_3)$	diag (378,922, 957,888, 994,747)
Telescopic link $k_2^{(3)}$	12.6	$B_3 + 57.5(A_3 - B_3))/\mathrm{norm}(A_3 - B_3)$	diag (83, 15,285, 15,288)
Swinging link $k_1^{(4)}$	674.3	$A_4 + 57.5(B_4 - A_4)/\mathrm{norm}(B_4 - A_4)$	diag (378,922, 957,888, 994,747)
Telescopic link $k_2^{(4)}$	12.6	$B_4 + 57.5(A_4 - B_4)/\mathrm{norm}(A_4 - B_4)$	diag (83, 15,285, 15,288)

In this study, step climbing is selected as a representative terrain that the biped robot needs to pass over during walking. The trajectory of the moving platform is shown in Figure 5a. As can be observed from the figure, while lifting its leg, the moving platform approaches the side of the fixed platform, then moves forward, and finally descends onto the step. By repeating this motion, the robot can traverse the step terrain.

Figure 5b,c respectively illustrates the linear velocity components and magnitude of the moving platform, while Figure 5d,e shows its linear acceleration components and magnitude. Owing to the continuity and smoothness of the trajectory generated by the quintic polynomial, the velocity and acceleration of the moving platform smoothly transition to zero at both the initial and final instants of motion. This effectively reduces the impact that occurs at the moments of leg lifting and ground contact during the motion of the dual-platform biped robot.

By substituting the trajectory equation of the moving platform into the kinematic models of the moving platform and each link, the driving velocity and acceleration of the dual-platform biped robot, as well as the CoM velocity and acceleration of all links, can be obtained, which serve as the basis for the subsequent driving forces numerical verification.

The theoretical results are validated through comparison with simulation results, as illustrated in Figure 6. Figure 6a–d, respectively, show the velocity comparison curves of actuators 1, 2, 3, and 4. Figure 6e presents the velocity error curves of the four branch chain actuators.

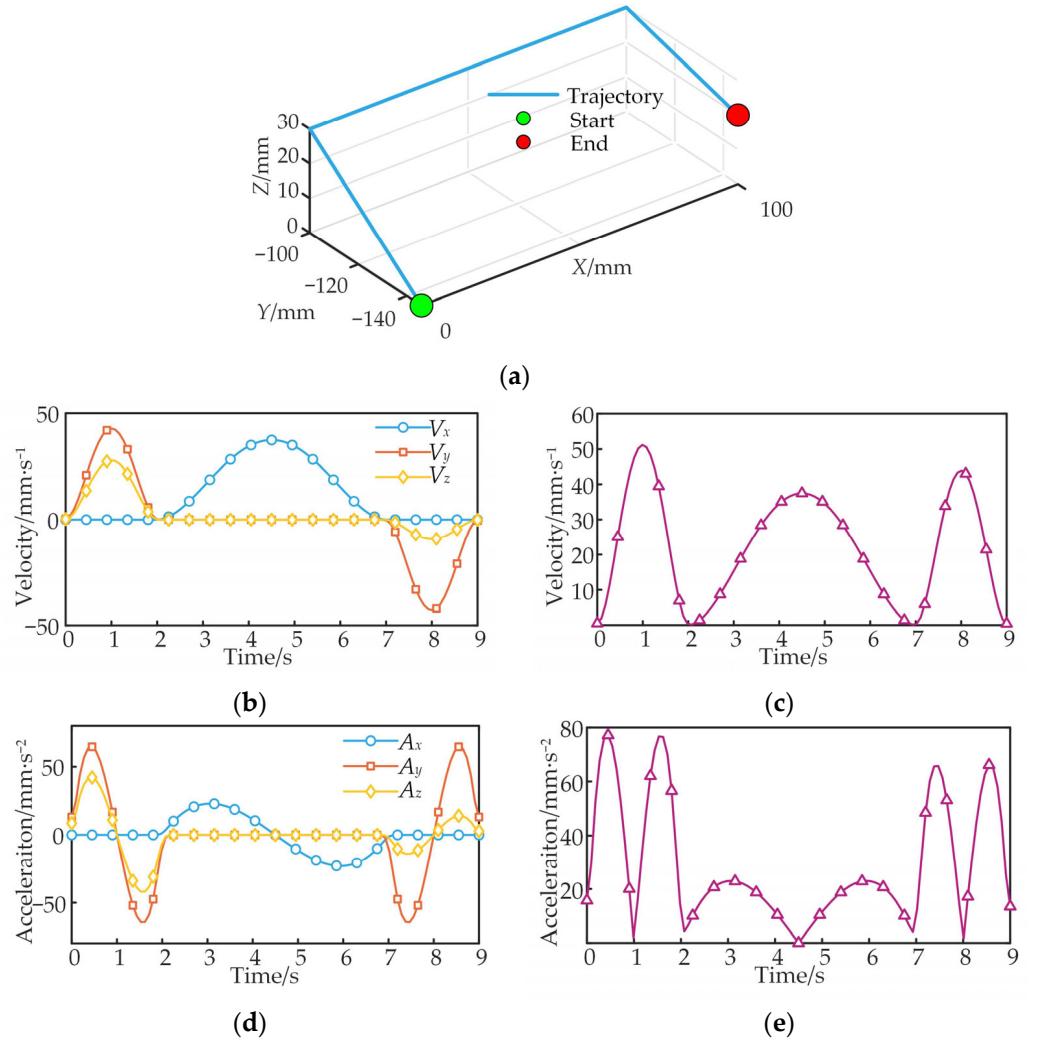


Figure 5. Motion pattern of the moving platform: (**a**) the trajectory of the moving platform; (**b**) the linear velocity components; (**c**) the linear velocity magnitude; (**d**) the linear acceleration components; and (**e**) the linear acceleration magnitude.

Figure 7a–d, respectively, illustrate the acceleration comparison curves of actuators 1, 2, 3, and 4. Figure 7e shows the acceleration error curves of the four branch chain actuators. The velocity and acceleration errors of all actuated joints reach their minimum value during the period of 2~7 s. This phenomenon occurs because, during the leg-lifting phase, the velocity and acceleration of the moving platform along the *Z*-axis are generated by two serial P branch chains. Compared with parallel mechanisms, serial chains generally exhibit lower motion accuracy, which results in a larger error during this interval. Nevertheless, the overall error magnitude remains within an acceptable range, with an error precision on the order of 10^{-1}. These results fully demonstrate the effectiveness of the influence coefficient method in determining the velocity and acceleration of the parallel mechanism and further verify the accuracy of the established kinematic model.

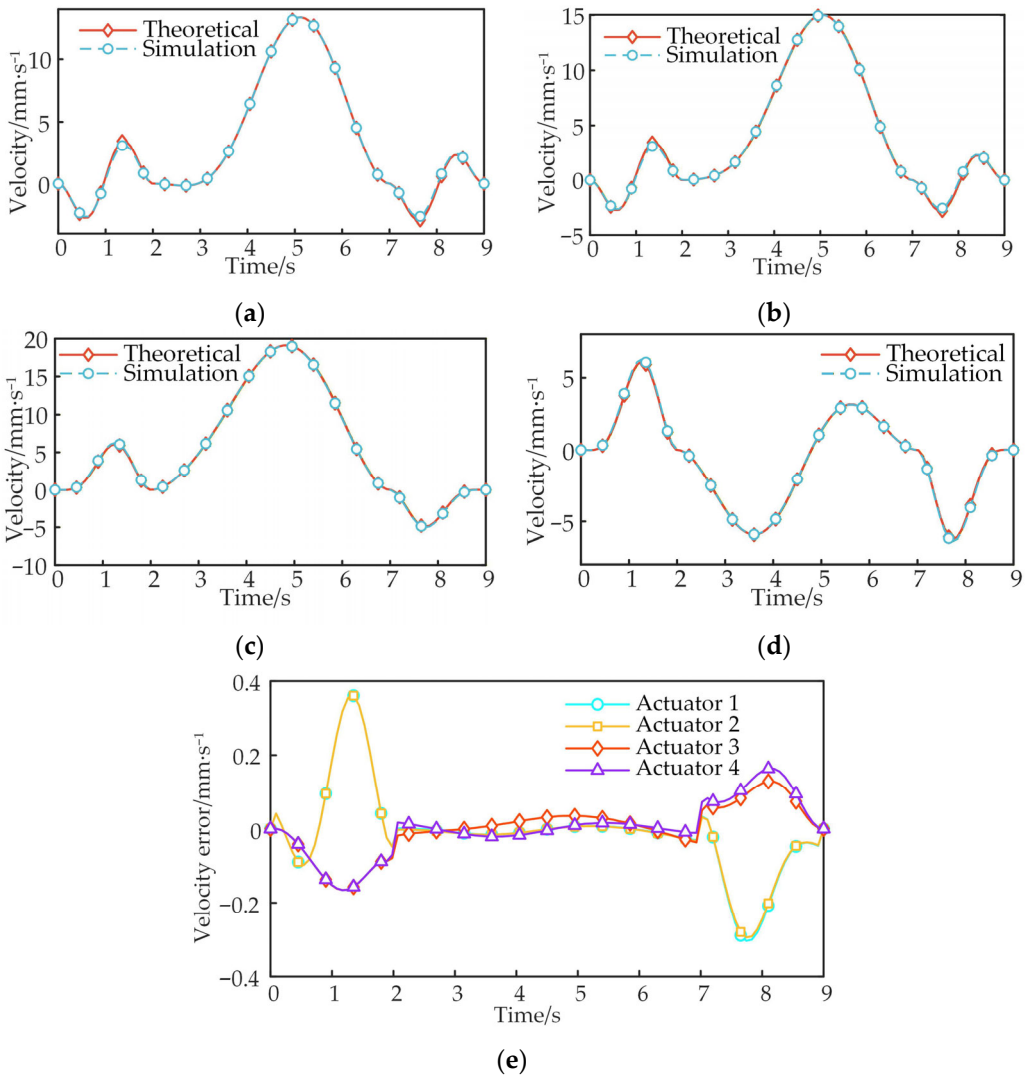


Figure 6. Velocity comparison curves and error curves: (**a**) Actuator 1; (**b**) Actuator 2; (**c**) Actuator 3; (**d**) Actuator 4; and (**e**) error curves.

Based on the prescribed trajectory of the moving platform and the dynamics model established in Section 3.2, the theoretical driving forces of all actuated joints in the dual-platform biped robot can be computed. Figure 8a,b presents the simulated driving forces of the robot's actuated joints and the theoretical driving forces obtained from the dynamics model in Section 3.2.

As shown by the comparison between Figure 8a,b, the simulated and theoretical values of the driving force show a strong agreement in their variation trends, and their magnitudes are nearly identical. Quantitative analysis shows that the maximum error does not exceed 5%, which is within the allowable range. The comparison results between the simulated and theoretical values fully validate the correctness of the dynamics model established in this paper, providing a reliable theoretical basis for subsequent performance evaluation and dynamic stability analysis of the dual-platform biped robot.

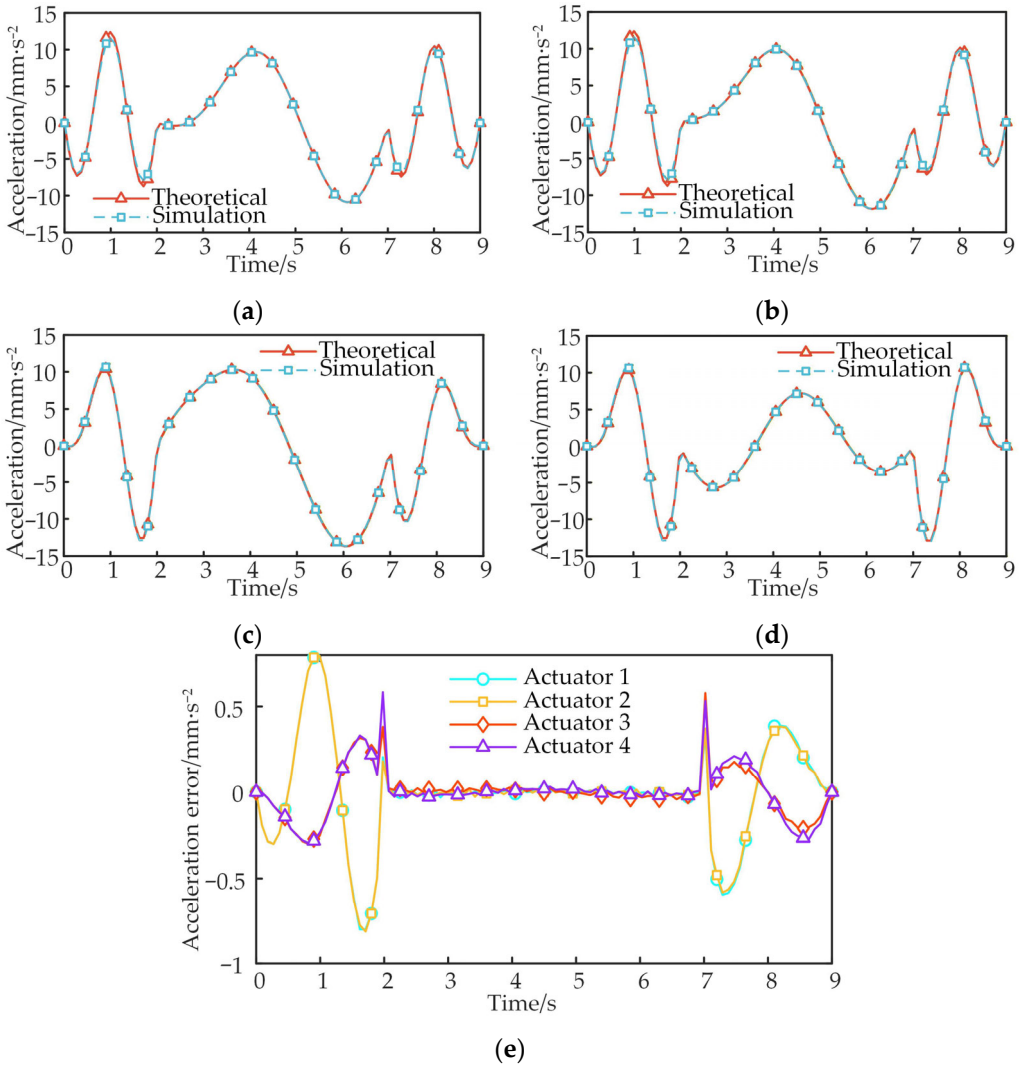


Figure 7. Acceleration comparison curves and error curves: (**a**) Actuator 1; (**b**) Actuator 2; (**c**) Actuator 3; (**d**) Actuator 4; and (**e**) error curves.

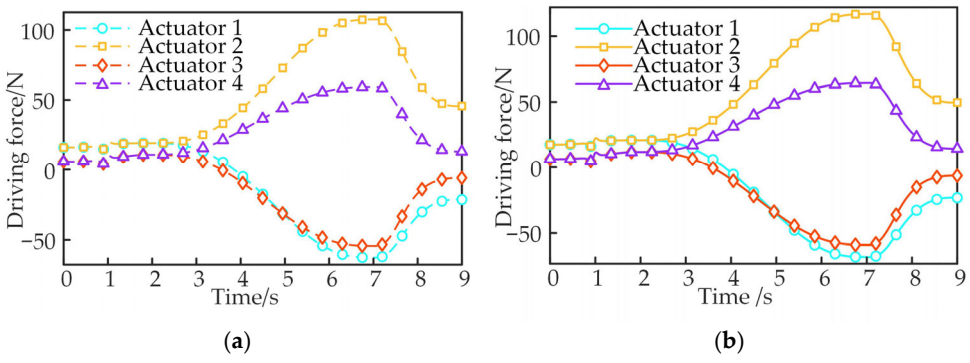


Figure 8. The simulation results are compared with the theoretical results: (**a**) simulation results of driving force; (**b**) theoretical results of driving force.

4. Dynamic Manipulability Ellipsoid Index

Performance analysis of mechanisms is a central topic in the field of robotics. At present, the DME index [32] is widely applied to evaluate the dynamic performance of parallel mechanisms. The dynamic manipulability of a robot refers to the ability of the moving platform to generate acceleration under fixed joint forces or torques, whereas the

dynamic manipulability ellipsoid describes the isotropy of this acceleration capability [33]. In this section, the ratio of the major to minor axes of the ellipsoid is adopted to evaluate the translational acceleration isotropy of the moving platform of the dual-platform biped robot at different positions and orientations. Furthermore, performance distribution maps are provided to visually demonstrate the effect of different lifting heights and rotational angles of the robot's foot on its dynamic manipulability.

Based on the mapping relationship between Euler angular velocity space and Cartesian angular velocity space, the relationship between the angular velocity of the moving platform end-effector of the dual-platform biped robot and the independent generalized velocities of the system can be derived as

$$\boldsymbol{\omega}_H = \begin{bmatrix} 0 & 0 & 0 & 0 \\ 0 & 0 & 0 & 0 \\ 1 & 0 & 0 & 0 \end{bmatrix} \dot{\boldsymbol{\eta}} = \boldsymbol{J}_{H,\mathrm{R}} \dot{\boldsymbol{\eta}} \tag{39}$$

where $\dot{\boldsymbol{\eta}} = \begin{bmatrix} \dot{\alpha} & \dot{X} & \dot{Y} & \dot{Z} \end{bmatrix}^{\mathrm{T}}$ denotes the independent generalized velocity vector of the dual-platform biped robot.

The linear velocity vector of the moving platform is given by

$$\boldsymbol{v}_H = \begin{bmatrix} 0 & 1 & 0 & 0 \\ 0 & 0 & 1 & 0 \\ 0 & 0 & 0 & 1 \end{bmatrix} \dot{\boldsymbol{\eta}} = \boldsymbol{J}_{H,\mathrm{T}} \dot{\boldsymbol{\eta}} \tag{40}$$

By combining Equations (13), (39), and (40), the mapping relationship between the driving velocity of the biped robot and the system's independent generalized velocities can be established as

$$\dot{\boldsymbol{q}} = \boldsymbol{J}_d \dot{\boldsymbol{\eta}} \tag{41}$$

where $\boldsymbol{J}_d = \boldsymbol{G}_H^q \boldsymbol{J}_H$, $\boldsymbol{J}_H = \begin{bmatrix} \boldsymbol{J}_{H,\mathrm{R}} & \boldsymbol{J}_{H,\mathrm{T}} \end{bmatrix}^{\mathrm{T}}$.

For the UPU branch chain i, substituting Equation (41) into Equation (16) and Equation (18) yields the mapping relationships between the CoM velocities of the swinging link k_1 and the telescopic link k_2, and the independent generalized velocities can be derived as

$$\begin{aligned} \boldsymbol{V}_{k1}^{(i)} &= \boldsymbol{J}_{k1}^{(i)} \dot{\boldsymbol{\eta}} \\ \boldsymbol{V}_{k2}^{(i)} &= \boldsymbol{J}_{k2}^{(i)} \dot{\boldsymbol{\eta}} \end{aligned} \tag{42}$$

where $\boldsymbol{J}_{k1}^{(i)} = \boldsymbol{G}_q^{k1} \boldsymbol{J}_d$, $\boldsymbol{J}_{k2}^{(i)} = \boldsymbol{G}_q^{k2} \boldsymbol{J}_d$.

To simplify the derivation of the DME index, the centrifugal, Coriolis, and gravitational terms in the dynamics analysis in Section 3.2 are neglected. Accordingly, the ellipsoidal expression representing the acceleration range of the moving platform along various directions under constrained driving forces is obtained as follows:

$$\|\boldsymbol{\tau}\| = \boldsymbol{A}_H^{\mathrm{T}} \boldsymbol{N}^{\mathrm{T}} \boldsymbol{N} \boldsymbol{A}_H \leq 1 \tag{43}$$

where $\boldsymbol{N} = \boldsymbol{J}_d^{+\mathrm{T}} \boldsymbol{H}^{\mathrm{T}} \boldsymbol{\zeta} \boldsymbol{H} \boldsymbol{J}_d^{+} \left[\boldsymbol{G}_q^H \right]^{+}$ denotes the inertia matrix of the system [34], $\boldsymbol{H}$ is the velocity Jacobian matrix relating the velocities of the moving components to the independent generalized velocities, and $\boldsymbol{\zeta}$ is the mass property matrix of the moving components. Here, $\boldsymbol{\zeta} = \mathrm{blkdiag}\left(I_{hc} \quad I_{k1}^{(1)} \quad \cdots \quad m_{k1}^{(4)} \quad m_{k2}^{(4)} \right)$, $\boldsymbol{H} = \begin{bmatrix} \boldsymbol{J}_{H,\mathrm{R}} & \boldsymbol{J}_{k1,R}^{(1)} & \cdots & \boldsymbol{J}_{k1,T}^{(4)} & \boldsymbol{J}_{k2,T}^{(4)} \end{bmatrix}^{\mathrm{T}}$.

Theoretically, the DME index can be decomposed into two sub-ellipsoids describing the isotropy of rotational and translational acceleration [35]. However, since the dual-platform biped robot possesses only one rotational DOF, namely rotation about the Z-axis,

the rotational sub-ellipsoid is not suitable for evaluating rotational acceleration isotropy. Focusing on translational acceleration isotropy, Equation (43) can be rearranged as

$$\|\boldsymbol{\tau}\| = \boldsymbol{A}_H^{\mathrm{T}} \boldsymbol{N}_{\mathrm{T}}^{\mathrm{T}} \boldsymbol{N}_{\mathrm{T}} \boldsymbol{A}_H \leq 1 \tag{44}$$

where $\boldsymbol{N}_{\mathrm{T}} = \boldsymbol{J}_d^{+\mathrm{T}} \boldsymbol{H}^{\mathrm{T}} \boldsymbol{\zeta} \boldsymbol{H} \boldsymbol{J}_d^{+} \left[\boldsymbol{G}_q^H \right]_{4:,5:,6:}^{+}$.

Based on the translational inertia matrix $\boldsymbol{N}_{\mathrm{T}}$ derived earlier, this paper adopts the reciprocal of the condition number of $\boldsymbol{N}_{\mathrm{T}}$ as the evaluation index, defining it as the quantitative index κ_{T} of translational acceleration isotropy of the dual-platform biped robot, and it can be expressed as

$$\kappa_{\mathrm{T}} = \frac{1}{\sqrt{\mathrm{Cond}(\boldsymbol{N}_{\mathrm{T}}^{\mathrm{T}} \boldsymbol{N}_{\mathrm{T}})}} \tag{45}$$

where $\mathrm{Cond}(\boldsymbol{N}_{\mathrm{T}}^{\mathrm{T}} \boldsymbol{N}_{\mathrm{T}})$ denotes the condition number of the matrix $\boldsymbol{N}_{\mathrm{T}}^{\mathrm{T}} \boldsymbol{N}_{\mathrm{T}}$.

Based on the structural parameters and mass properties of the dual-platform biped robot provided earlier, and according to Equation (45), the distribution of translational dynamic manipulability performance of Foot I at different lifting heights and rotation angles about the *Z*-axis is obtained, as shown in Figure 9. Here, the color represents the numerical value of the DME index.

Analysis of the translational dynamic manipulability performance distributions in Figure 9a–d shows that, when the rotation angle of the robot's foot about the *Z*-axis is fixed, the lifting height has no influence on the isotropy of translational acceleration. The reason is that the lifting motion of the foot is realized through two actuated P-branch chains, whose structure design ensures that changes in foot height do not alter the robot's translational acceleration characteristics. Moreover, the performance distribution diagrams reveal that the manipulability is symmetric with respect to the *Y*-axis. This indicates that the foot exhibits identical dynamic performance when moving forward and backward along the *X*-axis, which is consistent with the robot's front-back symmetric mechanical design.

In addition, when the foot position satisfies $Y \in [-250, -150]$ mm or $Y \in [-75, 25]$ mm, the isotropy of translational acceleration reaches its optimum. This phenomenon arises because the structural parameter design causes the biped robot to be close to singular regions when it is near its initial configuration. Consequently, in practical walking control, the relative distance between the two feet can be optimized to keep the foot within high-performance regions, thereby improving translational efficiency.

A comparison of Figure 9a with Figure 9e–h reveals that the translational acceleration isotropy of the dual-platform biped robot achieves its optimum when $\alpha = 10^\circ$. Moreover, as the rotation angle increases, the translational DME index first rises and then decreases. Therefore, to ensure favorable translational dynamic performance during practical walking, the robot's foot should avoid executing a large-angle rotation in a single step when turning. Instead, the rotation angle should be restricted within 15° per step, after which the remaining turning motion can be completed.

In summary, the above analysis shows that the translational acceleration performance of the dual-platform biped robot is unaffected by the lifting height but is sensitive to rotation about the Z-axis. The results confirm that structural design constrains the robot's dynamic performance near its initial configuration. By identifying the optimal workspace of the foot, the robot can achieve improved acceleration isotropy and enhanced locomotion efficiency, providing valuable guidance for stability control in complex terrains.

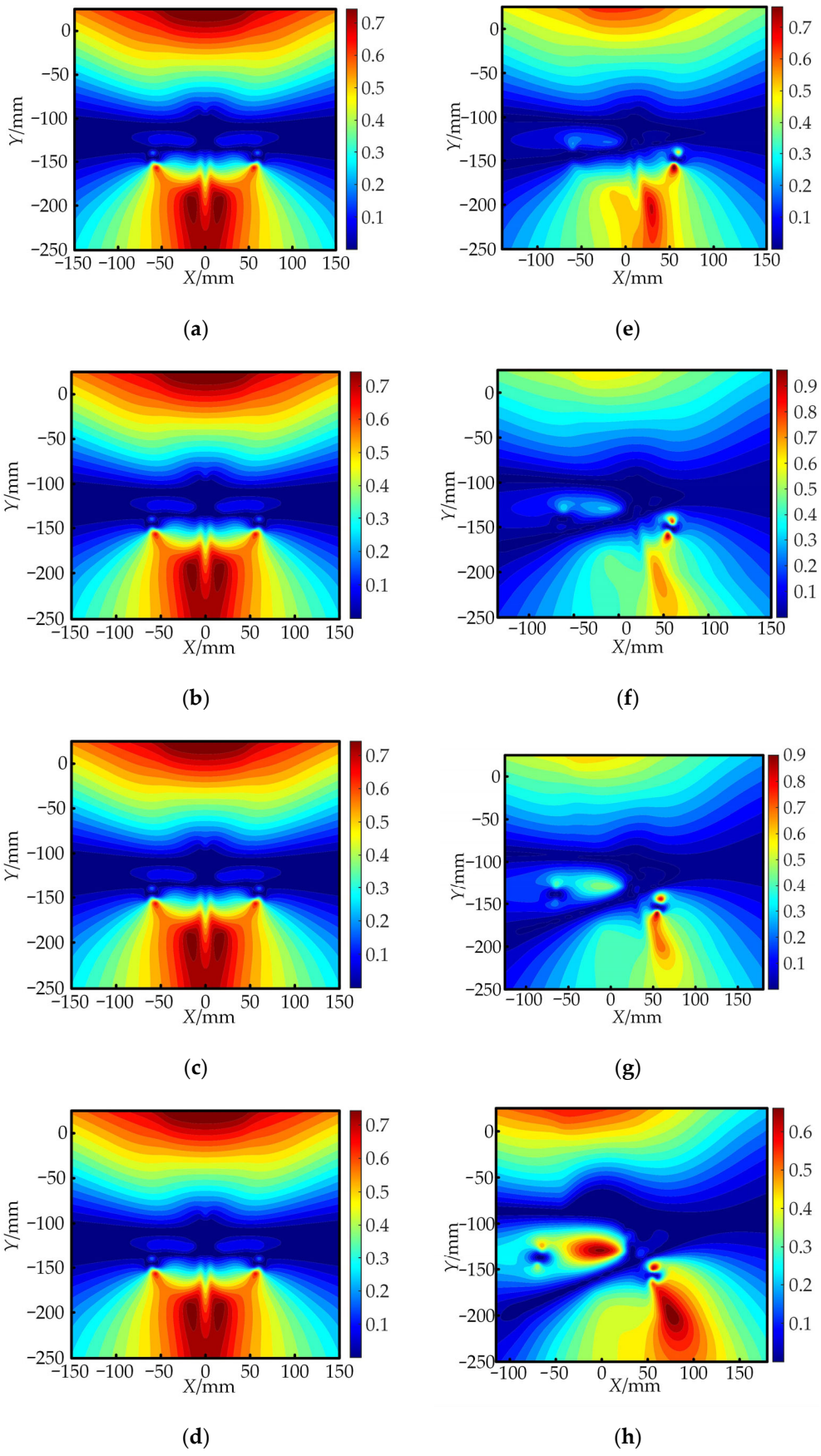


Figure 9. Distribution of the DME index at Foot I of the dual-platform biped robot at different heights and rotation angles: (**a**) Z = 10 mm, α = 0°; (**b**) Z = 20 mm, α = 0°; (**c**) Z = 30 mm, α = 0°; (**d**) Z = 40 mm, α = 0°; (**e**) Z = 10 mm, α = 5°; (**f**) Z = 10 mm, α = 10°; (**g**) Z = 10 mm, α = 15°; and (**h**) Z = 10 mm, α = 20°.

5. Dynamic Stability

Although the previous section focused on evaluating the dual-platform biped robot's DME, the robot requires not only good motion performance but also the ability to resist tipping during actual locomotion. Therefore, the following section analyzes the robot's dynamic stability.

When operating in dangerous and complex underground spaces such as pits, gullies, and steps, the dual-platform biped robot must achieve stable locomotion and avoid instability phenomena such as tipping over. Therefore, employing accurate performance indices to evaluate the stability of biped robots is of great significance for trajectory planning, structural parameter optimization, and control system design. Currently, the most used indices for assessing the dynamic stability of mobile robots include the Zero Moment Point and the Foot Rotation Indicator Point. The concept of the ZMP was first introduced by Vukobratovic et al. [36] and it is defined as the point within the contact region between the supporting foot and the ground where the resultant ground reaction force can be equivalently regarded as a single force acting at that point, with the corresponding moment equal to zero. This point is referred to as ZMP. Given that the ZMP method is well-suited for evaluating the dynamic stability of mobile robots walking on various unstructured terrains, this paper therefore adopts the ZMP approach and uses the moving platform's trajectory equations derived in Section 3.3 to simulate the step-climbing process of the biped robot, thereby assessing its dynamic stability, as illustrated in Figure 10.

In addition to simulating the step-climbing process, this study also performed simulations of the turning process of the dual-platform biped robot. Since the step-climbing simulation already includes the robot's flat-ground walking gait, the turning simulation presents only the foot-end rotation process, without illustrating the subsequent walk-out phase. The corresponding simulation process is shown on Figure 11. In fact, after the robot completes the rotation of both feet, the remaining walking process is the same as that in the step-climbing scenario, apart from the leg lift height. Therefore, it is not further elaborated here.

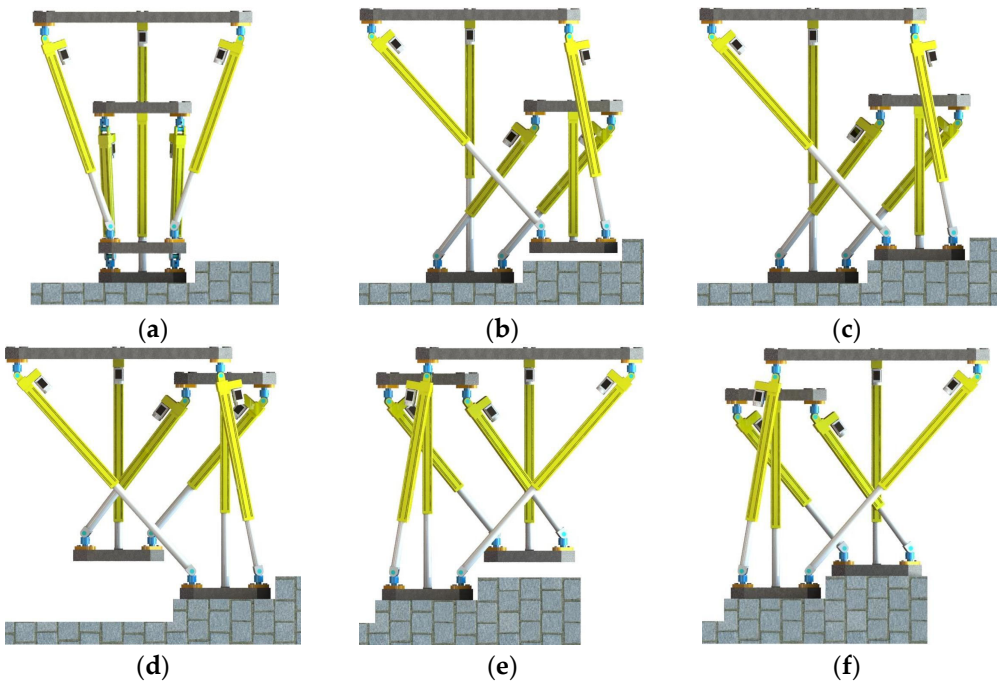


Figure 10. Gait pattern for step climbing: (**a**) lifting of Foot I and Platform I; (**b**) advance of Foot I and Platform II; (**c**) descent of Foot I and Platform I; (**d**) lifting of Foot II and Platform II; (**e**) advance of Foot II and Platform I; and (**f**) descent of Foot II and Platform II.

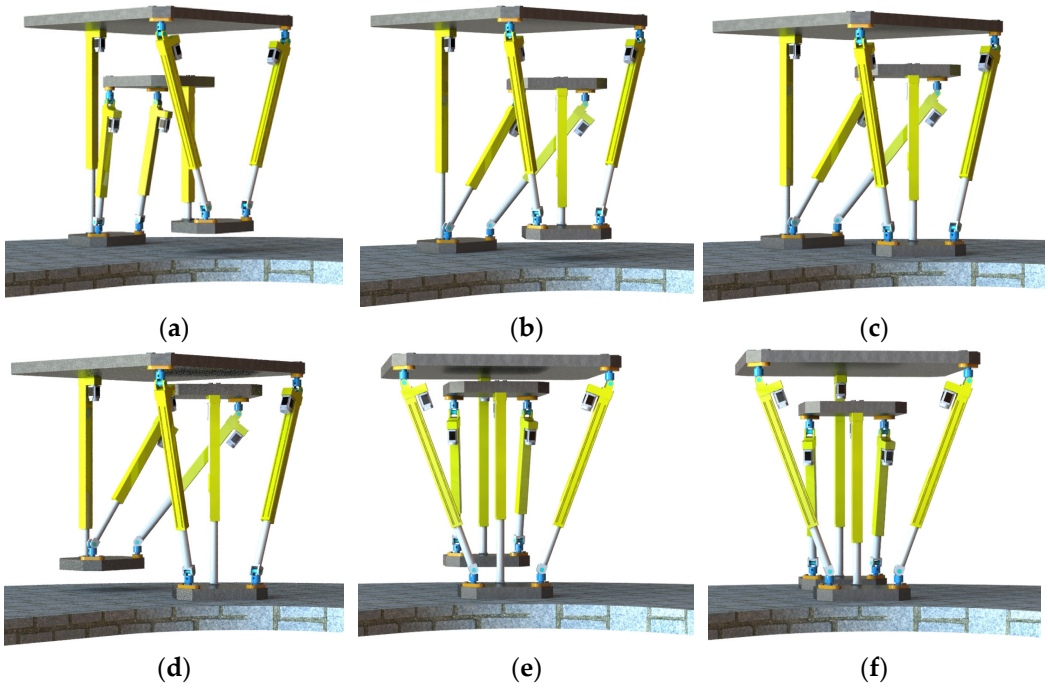


Figure 11. Gait pattern for turning: (**a**) lifting of Foot I and Platform I; (**b**) turning of Foot I and Platform II; (**c**) descent of Foot I and Platform I; (**d**) lifting of Foot II and Platform II; (**e**) turning of Foot II and Platform I; and (**f**) descent of Foot II and Platform II.

The ZMP stability criterion determines the dynamic stability of a mobile robot during locomotion based on the positional relationship between the ZMP and the support polygon. Here, the polygon formed by the contact between the supporting foot and the ground during walking is referred to as the support polygon. Figure 12 illustrates the geometric representation of the support polygon at different walking phases of the biped robot, where the solid lines denote the actual boundary of the support polygon. As the dual-platform biped robot alternates between single-foot support and biped support phases during walking, its biped feet and the ground together form a dynamically shifting support region with continuously varying boundaries. If the ZMP remains within the support region during walking, the condition of dynamic stability is satisfied, ensuring that the robot is experiencing stability. On the contrary, if the ZMP lies outside the support region, the robotic system will be in an unstable state.

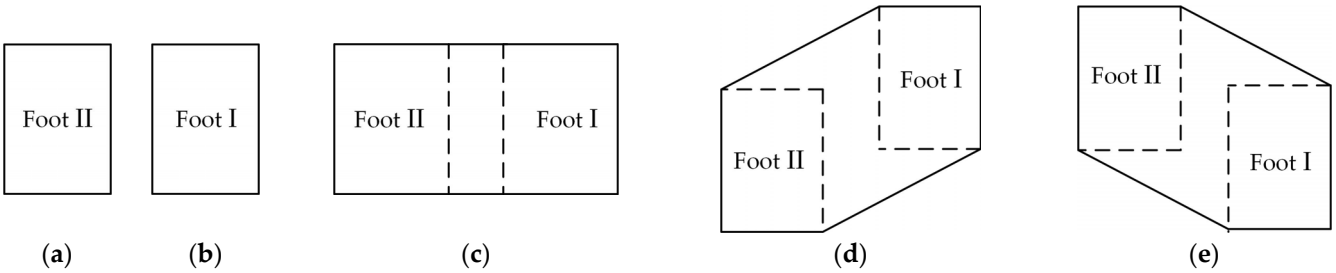


Figure 12. Support polygons during different gait phases: (**a**) Foot II support; (**b**) Foot I support; (**c**) bipedal support (in-line); (**d**) bipedal support (Foot I in front); and (**e**) bipedal support (Foot II in front).

According to Ref. [37], the formula for calculating the ZMP is given as follows:

$$\begin{cases} x_{\mathrm{ZMP}} = \dfrac{\sum_i m_i(\ddot{z}_i + g)x_i - \sum_i m_i \ddot{x}_i z_i}{\sum_i m_i(\ddot{z}_i + g)} \\ y_{\mathrm{ZMP}} = \dfrac{\sum_i m_i(\ddot{z}_i + g)y_i - \sum_i m_i \ddot{y}_i z_i}{\sum_i m_i(\ddot{z}_i + g)} \end{cases} \tag{46}$$

where (x_i, y_i, z_i) denote the coordinates of the CoM of the component i in the fixed coordinate system, while $(x_{\mathrm{ZMP}}, y_{\mathrm{ZMP}})$ represents the coordinates of the ZMP in the fixed coordinate system, and m_i represents the mass of the component i.

By simultaneously solving Equations (12), (16), (18), (23), (28), and (31), the accelerations of each component of the dual-platform biped robot during the entire walking process can be obtained. Substituting these results into Equation (46) yields the trajectory of the ZMP within the support region during the step-climbing process, as illustrated in Figure 13. In the figure, the support regions (a)~(e) at different walking phases correspond to the support polygons (a)~(e) shown in Figure 12, similarly hereinafter

Figure 13 shows an example of the ZMP trajectory generated based on Equation (46). As illustrated, the periodic step length is 70 mm, and the two foot-ends of the dual-platform biped robot remain parallel. The initial step width (i.e., the distance between centers of the two feet) is 146 mm. Throughout the entire step-climbing process, the robot's ZMP remains within the support region for approximately 80% of the time. Figure 13 also indicates that most instability states occur during the leg-lifting phase, which corresponds to the pose adjustment process, while the ZMP remains largely stable within the support region during forward motion. Therefore, while ensuring overall motion performance, the aim is to reduce the duration of the pose adjustment in the leg lifting phase so that the robot can return to a stable state as quickly as possible, thereby achieving steady walking.

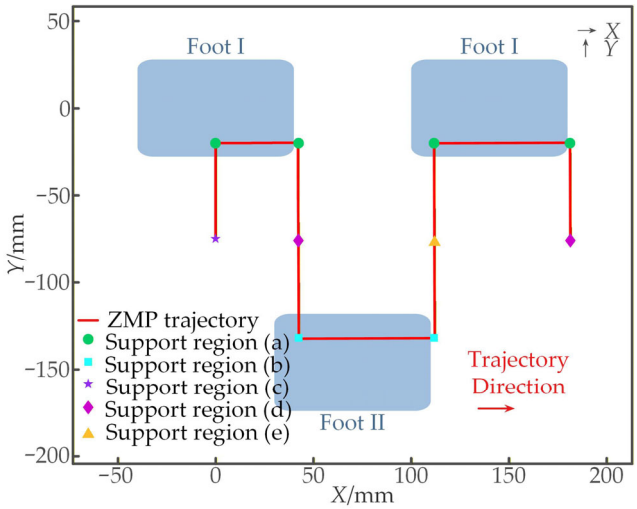


Figure 13. ZMP trajectory curve during robot step climbing.

By simultaneously solving Equations (12), (16), (18), (23), (28), and (31), and substituting the results into Equation (46), the ZMP trajectory curve of the biped robot during the turning process can be obtained, as shown in Figure 14. To more intuitively observe the ZMP trajectory during the turning process, the ZMP curves for the rotation of Foot II and Foot I are presented in two separate parts. In fact, there is no displacement along the X and Y axes of the feet; only rotation around the Z axis occurs.

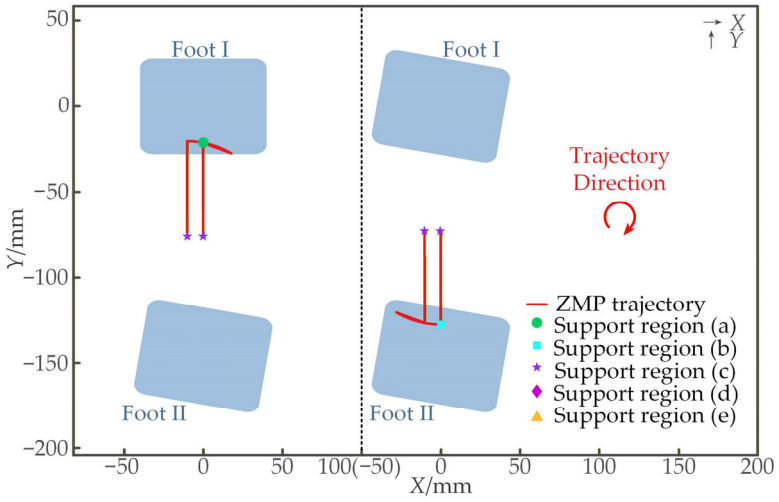


Figure 14. ZMP trajectory curve during robot turning.

Figure 14 shows an example of the ZMP trajectory generated by the dual-platform biped robot during the turning process based on Equation (46). As shown in the figure, in the initial pose, the two feet of the robot are parallel to each other. When the robot needs to pass through the curved terrain, the feet rotate sequentially. After completing the turning motion, the robot continues to move forward. Throughout the turning simulation, the ZMP of the robot remains within the support region except during the leg-lifting phase. This observation indicates that the dynamic stability of the robot during turning satisfies the stability requirements.

In summary, the dual-platform biped robot exhibits a certain level of dynamic stability in both step-climbing and turning simulations. Moreover, its stability during step-climbing can be further improved by appropriately adjusting the step-length parameters and optimizing the mass distribution.

6. Conclusions

This paper proposes a novel biped robot that achieves alternating leg motion solely through the switching of the moving and fixed platforms within a single parallel mechanism. This design effectively reduces the number of parallel mechanisms and actuators, thereby significantly lowering energy consumption and walking load. The main conclusions of this work are summarized as follows:

(1) A novel dual-platform biped robot based on a 4-UPU parallel mechanism is proposed. The robot ensures sufficient DOF while reducing the number of actuators and simplifying the leg structure, thereby minimizing energy consumption during locomotion.

(2) The velocity and acceleration mapping relationships between all moving components and actuators of the dual-platform biped robot were derived using the influence coefficient method. On this basis, an inverse dynamic model of the robot was established using the principle of virtual work. Furthermore, by comparing the simulated and theoretical results of the actuators, the correctness and effectiveness of the established kinematic and dynamic models were validated.

(3) The DME index was employed to evaluate the dynamic performance of the biped robot, and the workspace region with superior dynamic performance was identified. Finally, the ZMP method was applied to analyze the robot's dynamic stability during step-climbing and turning. The results demonstrate that the robot exhibits a certain level of dynamic stability in the step-climbing and turning process, thereby validating the rationality of the proposed structural design.

7. Limitations and Future Work

The main contribution of this work lies in proposing a dual-platform biped robot configuration, establishing its dynamics model, and conducting performance analyses. To focus on the derivation and validation of the robot's rigid body dynamics model, this paper inevitably introduces certain simplifying assumptions in the dynamics section. These assumptions may lead to discrepancies between simulation results and the physical prototype, potentially affecting the robot's real-world performance and limiting the fidelity of deployment on the prototype.

In response to the above limitations, this paper outlines a clear roadmap for future work aimed at progressively advancing the present dynamics model toward high-fidelity simulation and physical prototype realization.

(1) In forthcoming studies, we will develop a dynamics model that incorporates motor dynamics (including rotor inertia, back electromotive force, and electrical dynamics) and joint friction. This dynamics model will be used for future simulations and control system design, making the dynamics model more consistent with real physical constraints and providing a reliable foundation for prototype control.

(2) The core of future work is to deploy the simulation-validated control system on a physical prototype. By conducting walking experiments in real environments, such as step-climbing and turning locomotion, the feasibility and effectiveness of the proposed model will be further verified, providing both theoretical and practical support for the application of the dual-platform biped robot.

Author Contributions: Conceptualization, Z.S.; methodology, Z.S. and S.S.; validation, Z.S., R.L., and F.N.; writing—original draft preparation, Z.S., S.S., and L.Z.; writing—review and editing, Z.S., S.S., R.L., and L.D.; supervision, S.S.; funding acquisition, S.S. All authors have read and agreed to the published version of the manuscript.

Funding: This research was funded by the Key Research and Development Program of Shanxi Province of China, grant number 202202150401018.

Data Availability Statement: Data is contained within this article.

Conflicts of Interest: The authors declare no conflicts of interest.

Abbreviations

The following abbreviations are used in this manuscript:

DME	Dynamic Manipulability Ellipsoid
ZMP	Zero-Moment Point
DOF	Degree of freedom
CoM	Center-of-mass
R	Revolute joint
P	Prismatic joint
S	Spherical joint
U	Universal joint

References

1. Huang, D.H.; Fan, W.; Liu, Y.; Liu, T. Design of a Humanoid Bipedal Robot Based on Kinematics and Dynamics Analysis of Human Lower Limbs. In Proceedings of the 2020 IEEE/ASME International Conference on Advanced Intelligent Mechatronics (AIM), Boston, MA, USA, 6–9 July 2020; IEEE: Piscataway, NJ, USA, 2020. [CrossRef]
2. Shin, H.; Ishikawa, T.; Kamioka, T.; Hosoda, K.; Yoshiike, T. Mechanistic Properties of Five-Bar Parallel Mechanism for Leg Structure Based on Spring Loaded Inverted Pendulum. In Proceedings of the 2019 IEEE-RAS 19th International Conference on Humanoid Robots (Humanoids), Toronto, ON, Canada, 15–17 October 2019; IEEE: Piscataway, NJ, USA, 2020. [CrossRef]

3. Zade, H.; Varude, A.; Pandya, K.; Kamat, A.; Chiddarwar, S.; Thakker, R. ReQuBiS—Reconfigurable Quadrupedal-Bipedal Snake Robots. In Proceedings of the 2021 IEEE 17th International Conference on Automation Science and Engineering (CASE), Lyon, France, 23–27 August 2021; IEEE: Piscataway, NJ, USA, 2021. [CrossRef]
4. Yang, X.; She, H.T.; Lu, H.J.; Fukuda, T.; Shen, Y.J. State of the Art: Bipedal Robots for Lower Limb Rehabilitation. *Appl. Sci.* **2017**, *7*, 1182. [CrossRef]
5. Iotti, F.; Ranjan, A.; Angelini, F.; Garabini, M. OmniQuad: A Wheeled-Legged Hybrid Robot with Omnidirectional Wheels. *Mech. Mach. Theory* **2025**, *214*, 106125. [CrossRef]
6. Chen, Z.J.; Xi, Q.X.; Qi, C.K.; Chen, X.B.; Gao, Y.; Gao, F. Fault-Tolerant Gait Design for Quadruped Robots with Two Locked Legs Using the GF Set Theory. *Mech. Mach. Theory* **2024**, *195*, 105592. [CrossRef]
7. Mazumdar, A.; Spencer, S.J.; Hobart, C.; Salton, J.; Quigley, M.; Wu, T.F.; Bertrand, S.; Pratt, J.; Buerger, S.P. Parallel Elastic Elements Improve Energy Efficiency on the STEPPR Bipedal Walking Robot. *IEEE/ASME Trans. Mechatron.* **2017**, *22*, 898–908. [CrossRef]
8. Kumar, M.; Gautam, P.; Semwal, V.B. A Review of Computational Model for Bipedal Robot Walking Using Gait Analysis. In Proceedings of the 2020 International Conference on Emerging Smart Computing and Informatics (ESCI), Pune, India, 12–14 March 2020; IEEE: Piscataway, NJ, USA, 2020. [CrossRef]
9. Yao, D.J.; Yang, L.; Xiao, X.H.; Zhou, M.C. Velocity-Based Gait Planning for Underactuated Bipedal Robot on Uneven and Compliant Terrain. *IEEE Trans. Ind. Electron.* **2022**, *69*, 11414–11424. [CrossRef]
10. Taheri, H.; Mozayani, N. A Study on Quadruped Mobile Robots. *Mech. Mach. Theory* **2023**, *190*, 105448. [CrossRef]
11. Mikolajczyk, T.; Mikołajewska, E.; Al-Shuka, H.F.N.; Malinowski, T.; Kłodowski, A.; Pimenov, D.Y.; Paczkowski, T.; Hu, F.W.; Giasin, K.; Mikołajewski, D.; et al. Recent Advances in Bipedal Walking Robots: Review of Gait, Drive, Sensors and Control Systems. *Sensors* **2022**, *22*, 4440. [CrossRef]
12. Mou, H.M.; Tang, J.; Liu, J.; Xu, W.Q.; Hou, Y.F.; Zhang, J.W. High Dynamic Bipedal Robot with Underactuated Telescopic Straight Legs. *Mathematics* **2024**, *12*, 600. [CrossRef]
13. Zhang, Y.; Zang, X.; Chen, B.Y.; Zhang, X.H.; Liu, Y.B.; Zhao, J. Type Synthesis of a Novel 4-Degrees-of-Freedom Parallel Bipedal Mechanism for Walking Robot. *Adv. Intell. Syst.* **2024**, *6*, 2300384. [CrossRef]
14. Xie, Z.Q.; Wang, Y.L.; Luo, X.; Arpenti, P.; Ruggiero, F.; Siciliano, B. Three-Dimensional Variable Center of Mass Height Biped Walking Using a New Model and Nonlinear Model Predictive Control. *Mech. Mach. Theory* **2024**, *197*, 105651. [CrossRef]
15. Wang, W.J.; Cai, S.T.; Hu, J.T.; Yang, X.F.; Lu, H.R.; Li, W.J. Design of A Bipedal Robot via Modular Actuator. In Proceedings of the 2022 International Conference on Advanced Robotics and Mechatronics (ICARM), Guilin, China, 9–11 July 2022; IEEE: Piscataway, NJ, USA, 2020. [CrossRef]
16. Liu, J.; Zhao, D.; Xing, J.D.; Zhang, B.Z.; Jiang, S. Design and Motion Analysis of a Leg Mechanism of an Unmanned Deformable Vehicle. *Struct Multidiscip. Optim.* **2025**, *68*, 121. [CrossRef]
17. Liang, Y.P.; Yin, F.L.; Li, Z.; Xiong, Z.L.; Peng, Z.H.; Zhao, Y.Z.; Yan, W.X. Reduced-Dimensional Whole-Body Control Based on Model Simplification for Bipedal Robots with Parallel Mechanisms. *IEEE Robot. Autom. Lett.* **2025**, *10*, 1696–1703. [CrossRef]
18. Demirel, M.; Kiper, G.; Carbone, G.; Ceccarelli, M. Design of a Novel Hybrid Cable-Constrained Parallel Leg Mechanism for Biped Walking Machines. *Robotica* **2023**, *41*, 1778–1793. [CrossRef]
19. Sugahara, Y.; Carbone, G.; Hashimoto, K.; Ceccarelli, M.; Lim, H.-O.; Takanishi, A. Experimental Stiffness Measurement of WL-16RII Biped Walking Vehicle During Walking Operation. *J. Robot. Mechatron.* **2007**, *19*, 272–280. [CrossRef]
20. Wang, R.C.; Lu, Z.G.; Xiao, Y.H.; Zhao, Y.H.; Jiang, Q.J.; Shi, X.H. Design and Control of a Multi-Locomotion Parallel-Legged Bipedal Robot. *IEEE Robot. Autom. Lett.* **2024**, *9*, 1993–2000. [CrossRef]
21. Tazaki, Y. Parallel Link-Based Light-Weight Leg Design for Bipedal Robots. In Proceedings of the 2019 IEEE-RAS 19th International Conference on Humanoid Robots (Humanoids), Toronto, ON, Canada, 15–17 October 2019; IEEE: Piscataway, NJ, USA, 2020. [CrossRef]
22. Gim, K.G.; Kim, J.; Yamane, K. Design and Fabrication of a Bipedal Robot Using Serial-Parallel Hybrid Leg Mechanism. In Proceedings of the 2018 IEEE/RSJ International Conference on Intelligent Robots and Systems (IROS), Madrid, Span, 1–5 October 2018; IEEE: Piscataway, NJ, USA, 2019. [CrossRef]
23. Xia, Z.H.; Zhang, D.; Chen, Y.Y.; Tian, C.X.; Liu, J.; Wu, C.W. A Novel 6 DOFs Generalized Parallel Manipulator Design and Analysis Based on Humanoid Leg. *Mech. Mach. Theory* **2022**, *176*, 105029. [CrossRef]
24. Li, R.Q.; Meng, H.W.; Bai, S.P.; Yao, Y.Y.; Zhang, J.W. Stability and Gait Planning of 3-UPU Hexapod Walking Robot. *Robotics* **2018**, *7*, 48. [CrossRef]
25. Ren, H.H.; Guo, X.J.; He, M.Z.B.; Ma, C.S.; Su, C.Z. Gait Optimization Method for a Large Heavy Load Biped Robot Based on Particle Swarm Optimizer Algorithm. *IEEE Access* **2024**, *12*, 172234–172243. [CrossRef]
26. Li, R.Q.; Hu, W.W.; Wang, C.Z.; Ning, F.P. Configuration Innovation and Stability Analysis of a Hexapod Load-Bearing Mountain Climbing Robot XuanGui. In Proceedings of the 2024 6th International Conference on Reconfigurable Mechanisms and Robots (ReMAR), Chicago, IL, USA, 23–26 June 2024; IEEE: Piscataway, NJ, USA, 2024. [CrossRef]

27. Gabardi, M.; Solazzi, M.; Frisoli, A. An Optimization Procedure Based on Kinematics Analysis for the Design Parameters of a 4-UPU Parallel Manipulator. *Mech. Mach. Theory* **2019**, *133*, 211–228. [CrossRef]
28. Thomas, M.; Tesar, D. Dynamic Modeling of Serial Manipulator Arms. *J. Dyn. Syst. Meas. Control* **1982**, *104*, 218–228. [CrossRef]
29. Zhang, L.; Li, R.Q.; Ning, F.P.; Chai, C.; Jia, Z.Y. Performance Analysis and Optimization Design of a Dual-Mode Reconfigurable Ankle Joint Parallel Rehabilitation Mechanism. *Appl. Sci.* **2024**, *14*, 1757. [CrossRef]
30. Zhang, X.C.; Rong, Y.; Wang, H.B.; Zhang, S.J. Kinematics and Dynamics Analysis of a New 5-Degrees of Freedom Parallel Mechanism with Two Double-Driven Chains. *Machines* **2025**, *13*, 419. [CrossRef]
31. Zhao, J.S.; Sun, X.C.; Wei, S.T. Kinematics and Dynamics Analysis of a 3UPS-UPU-S Parallel Mechanism. *Machines* **2023**, *11*, 840. [CrossRef]
32. Yoshikawa, T. Dynamic Manipulability of Robot Manipulators. *Trans. Soc. Instrum. Control Eng.* **1985**, *21*, 970–975. [CrossRef]
33. Sun, T.Z.; Ye, W.; Yang, C.; Huang, F.L. Dynamic Modeling and Performance Analysis of the 2PRU-PUU Parallel Mechanism. *Mech. Sci.* **2024**, *15*, 249–256. [CrossRef]
34. Chen, M.; Zhang, Q.; Qin, X.R.; Sun, Y.T. Kinematic, Dynamic, and Performance Analysis of a New 3-DOF over-Constrained Parallel Mechanism without Parasitic Motion. *Mech. Mach. Theory* **2021**, *162*, 104365. [CrossRef]
35. Yoehikawa, T. Translational and Rotational Manipulability Ot Robotic Manipulators. In Proceedings of the 1990 American control conference, San Diego, CA, USA, 23–25 May 1990; IEEE: Piscataway, NJ, USA, 2009. [CrossRef]
36. Vukobratović, M.; Borovac, B. Zero-Moment Point—Thirty Five Years of Its Life. *Int. J. Humanoid Robot.* **2004**, *01*, 157–173. [CrossRef]
37. Borovac, B.; Nikolić, M.; Raković, M.; Savić, S. ZMP—Where Are We After Fifty-Five Years? *Int. J. Humanoid Robot.* **2024**, *21*, 2350030. [CrossRef]

Disclaimer/Publisher's Note: The statements, opinions and data contained in all publications are solely those of the individual author(s) and contributor(s) and not of MDPI and/or the editor(s). MDPI and/or the editor(s) disclaim responsibility for any injury to people or property resulting from any ideas, methods, instructions or products referred to in the content.